CEE'07 - 2nd INTERNATIONAL CONFERENCE ON ELECTRICAL ENGINEERING
ISBN: 978-972-99064-4-2

APPLICATIONS OF FRACTIONAL CALCULUS IN ELECTRICAL AND COMPUTER ENGINEERING

J. A. Tenreiro Machado [(1)], Manuel F. Silva [(1)], Ramiro S. Barbosa [(1)], Isabel S. Jesus [(1)], Cecília Reis [(1)], Maria G. Marcos [(1)], Luís M. Afonso [(1)], Miguel F. M. Lima [(2)], E. J. Solteiro Pires [(3)], N. M. Fonseca Ferreira [(4)]

[(1)] Institute of Engineering of Porto, Porto, Portugal, {jtm,mss,rsb,isj,cmr,mgm,lma}@isep.ipp.pt
[(2)] School of Technology of Viseu, Viseu, Portugal, lima@mail.estv.ipv.pt
[(3)] University of Trás-os-Montes and Alto Douro, Vila Real, Portugal, epires@utad.pt
[(4)] Institute of Engineering of Coimbra, Coimbra, Portugal, nunomig@isec.pt

Fractional Calculus (FC) goes back to the beginning of the theory of differential calculus. Nevertheless, the application of FC just emerged in the last two decades, due to the progress in the area of chaos that revealed subtle relationships with the FC concepts. In the field of dynamical systems theory some work has been carried out but the proposed models and algorithms are still in a preliminary stage of establishment. Having these ideas in mind, the paper discusses a FC perspective in the study of the dynamics and control of several systems. This article illustrates several applications of fractional calculus in science and engineering. It has been recognized the advantageous use of this mathematical tool in the modeling and control of many dynamical systems. In this perspective, this paper investigates the use of FC in the fields of controller tuning, electrical systems, digital circuit synthesis, evolutionary computing, redundant robots, legged robots, robotic manipulators, nonlinear friction and financial modeling.

Keywords: **fractional calculus, modelling, dynamics.**

1. Introduction

The generalization of the concept of derivative $D^{\alpha}[f(x)]$ to non-integer values of α goes back to the beginning of the theory of differential calculus. In fact, Leibniz, in his correspondence with Bernoulli, L'Hôpital and Wallis (1695), had several notes about the calculation of $D^{1/2}[f(x)]$. Nevertheless, the development of the theory of Fractional Calculus (*FC*) is due to the contributions of many mathematicians such as Euler, Liouville, Riemann and Letnikov [1-3].

The FC deals with derivatives and integrals to an arbitrary order (real or, even, complex order). The mathematical definition of a derivative/integral of fractional order has been the subject of several different approaches [1-3]. For example, the Laplace definition of a fractional derivative/integral of a signal $x(t)$ is:

$$D^{\alpha}x(t) = L^{-1}\left\{ s^{\alpha}X(s) - \sum_{k=0}^{n-1} s^{k} D^{\alpha-k-1}x(t)\Big|_{t=0} \right\} \qquad (1)$$

where $n-1 < \alpha \le n$, $\alpha > 0$. The Grünwald-Letnikov definition is given by ($\alpha \in \Re$):

$$D^{\alpha}x(t) = \lim_{h\to 0}\left[\frac{1}{h^{\alpha}} \sum_{k=0}^{\infty} (-1)^{k} \binom{\alpha}{k} x(t-kh) \right] \qquad (2a)$$

$$\binom{\alpha}{k} = \frac{\Gamma(\alpha+1)}{\Gamma(k+1)\Gamma(\alpha-k+1)} \qquad (2b)$$

where Γ is the Gamma function and h is the time increment. Equation (2) shows that fractional-order operators are "global" operators having a memory of all past events, making them adequate for modeling memory effects in most materials and systems.

Based on the proposed definitions it is possible to calculate the fractional-order integrals/derivatives of several functions (Table 1). Nevertheless, the problem of devising and implementing fractional-order algorithms is not trivial and will be the matter of the next sections.

Table 1- fractional-order integrals of several functions.

$\varphi(x),\ x \in \Re$	$\left(I_{+}^{\alpha}\varphi\right)(x),\ x \in \Re,\ \alpha \in C$
$(x-a)^{\beta-1}$	$\frac{\Gamma(\beta)}{\Gamma(\alpha+\beta)}(x-a)^{\alpha+\beta-1},\ \mathrm{Re}(\beta)>0$
$e^{\lambda x}$	$\lambda^{-\alpha}e^{\lambda x},\ \mathrm{Re}(\lambda)>0$
$\begin{cases}\sin(\lambda x)\\ \cos(\lambda x)\end{cases}$	$\lambda^{-\alpha}\begin{cases}\sin(\lambda x-\alpha\pi/2)\\ \cos(\lambda x-\alpha\pi/2)\end{cases},\ \lambda>0, \mathrm{Re}(\alpha)>1$
$e^{\lambda x}\begin{cases}\sin(\gamma x)\\ \cos(\gamma x)\end{cases}$	$\frac{e^{\lambda x}}{(\lambda^2+\gamma^2)^{\alpha/2}}\begin{cases}\sin(\gamma x-\alpha\phi)\\ \cos(\gamma x-\alpha\phi)\end{cases},\ \phi=\arctan(\gamma/\lambda)$, $\gamma>0, \mathrm{Re}(\lambda)>1$

In recent years fractional calculus (FC) has been a fruitful field of research in science and engineering [1-6]. In fact, many scientific areas are currently paying attention to the FC concepts and we can refer its adoption in viscoelasticity and damping, diffusion and wave propagation, electromagnetism, chaos and fractals, heat transfer, biology,

electronics, signal processing, robotics, system identification, traffic systems, genetic algorithms, percolation, modeling and identification, telecommunications, chemistry, irreversibility, physics, control systems, economy and finance.

Bearing these ideas in mind, sections 2 to 12 present several applications of FC in science and engineering. In section 13 we draw the main conclusions.

2. Van Der Pol oscillator of fractional order

The study of nonlinear oscillators has been important in the development of the theory of dynamical systems. The Van der Pol oscillator (VPO), described by a second-order nonlinear differential equation, can be regarded as describing a mass-spring-damper system with a nonlinear position-dependent damping coefficient or, equivalently, an RLC electrical circuit with a negative-nonlinear resistor, and has been used for developing models in many applications, such as electronics, biology or acoustics.

In the standard form, it is given by a second-order nonlinear differential equation of type:

$$\ddot{x} + \alpha\left(x^2 - 1\right)\dot{x} + x = 0 \tag{3}$$

or, in state-space form, as:

$$\begin{bmatrix} \dot{x}_1 \\ \dot{x}_2 \end{bmatrix} = \begin{bmatrix} 0 & 1 \\ -1 & -\alpha\left(x_1^2 - 1\right) \end{bmatrix} \begin{bmatrix} x_1 \\ x_2 \end{bmatrix} \tag{4}$$

where $\alpha > 0$ is the control parameter that reflects the degree of nonlinearity of the system. Equation (3) possesses a periodic solution that attracts other solution except the trivial one at the unique equilibrium point $x = \dot{x} = 0$.

A fractional version is now considered by introducing a fractional time derivative of order λ in state space equations (4) of the standard VPO, yielding [7]:

$$\begin{bmatrix} x_1^{(\lambda)} \\ \dot{x}_2 \end{bmatrix} = \begin{bmatrix} 0 & 1 \\ -1 & -\alpha\left(x_1^2 - 1\right) \end{bmatrix} \begin{bmatrix} x_1 \\ x_2 \end{bmatrix} \tag{5}$$

which corresponds to the differential equation:

$$x^{(1+\lambda)} + \alpha\left(x^2 - 1\right)x^{(\lambda)} + x = 0, \quad 0 < \lambda < 1 \tag{6}$$

Note that system (6) reduces to the classical VPO equation (3) when $\lambda = 1$ and that the total system order is changed to $\lambda+1 < 2$.

Figure 1 illustrates the block diagram representation of system (6). As can be seen, the fractional VPO system is implemented by using a fractional integrator $1/s^{\lambda}$ of order $0 < \lambda < 1$. The fractional-order integrator is an irrational transfer function in the Laplace s-variable. This type of systems has an unlimited memory which precludes its direct utilization in time-domain simulations. Therefore, the usual approach is the development of integer-order approximations that approximate (up to a given degree of accuracy) the fractional-order operators. So, in order to effectively analyze the fractional-order system of Fig. 1, we develop rational approximations for the fractional-order integrator $1/s^{\lambda}$. In this perspective, we adopt the approximation frequency method described by [8], known as "Singularity Function Method". These approximations were obtained for $\lambda \in]0,\ 1[$, frequency range of $\omega = [0.01,\ 100]$ rad/s and a maximum discrepancy from the ideal response of $\Delta = 2$ dB.

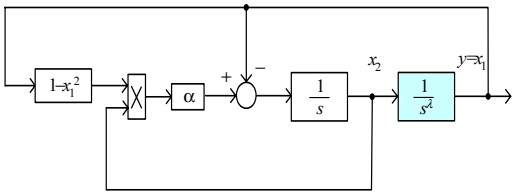

Figure 1 - block diagram of the fractional Van der Pol system.

Figure 2 shows the phase portraits for initial conditions $x_1(0) = 0$ and $x_2(0) = 1$ as the fractional-order λ (Fig. 2a)) and the control parameter α (Fig. 2b) are varied, respectively. In both cases, we verify significant variations of the limit cycle, revealing a large impact of the λ-order derivative upon system dynamics. In order to clarify this point, Fig. 3 illustrates the amplitude A and the period T of the output oscillation. It is clearly seen the large variation of the limit cycle, particularly in the period of the oscillation.

Figure 4 shows the steady-state time responses and the Fourier spectra of the output $x_1(t)$ for several values of λ and for $\alpha = 5$. The frequency spectrum was evaluated by using the FFT over $N = 2^{15}$ points after elapsing the initial transient of the signal output $x_1(t)$. Once more, we observe the variation of the limit cycle as function of λ, noting that the amplitude gets smaller as λ is decreased. On the other hand, analysing the Fourier spectra, we verify that the multiplicity of peaks and the amplitude of these peaks varies with α, which is in accordance with the time responses. Also note that the energy of the output signal, is not only concentrated in the peaks (fundamental and integer-odd harmonics), but distributed along all frequency domain, showing a long-term behaviour indicating different amplitude decays depending on λ [7].

The results reveal that the fractional version of the VPO system can exhibit different behaviour from those obtained with the standard Van der Pol oscillator depending on order's derivative (or system's order). The fractional-order can act as a

ISBN: 978-972-99064-4-2

modulation parameter that may be useful for a better understanding and control of such systems.

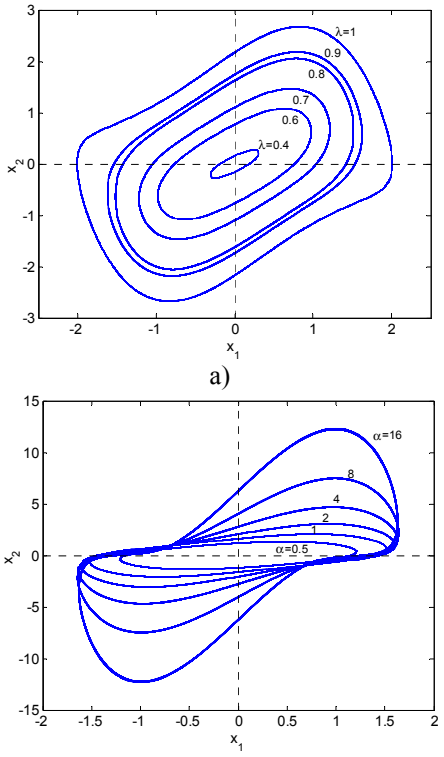

Figure 2 - phase portraits: a) $\lambda = \{0.4, 0.6, 0.7, 0.8, 0.9, 1.0\}$ and $\alpha = 1$, b) $\lambda = 0.8$ and $\alpha = \{0.5, 1, 2, 4, 8, 16\}$.

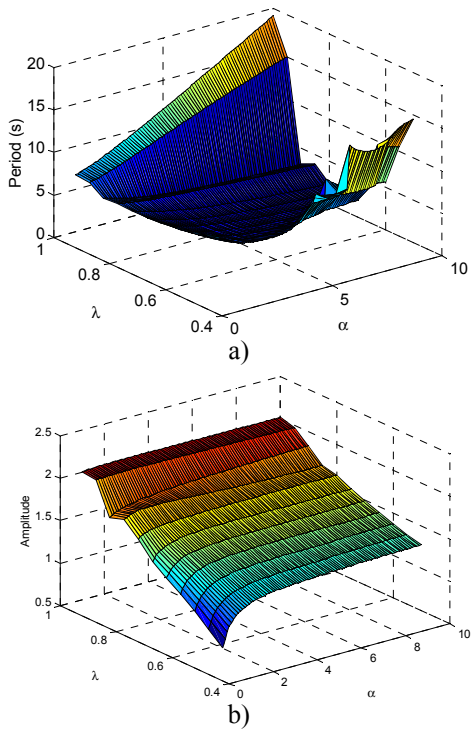

Figure 3 - limit cycle: a) period and b) amplitude of the output oscillation for $1 \leq \alpha \leq 10$ and $0.5 \leq \lambda \leq 1$.

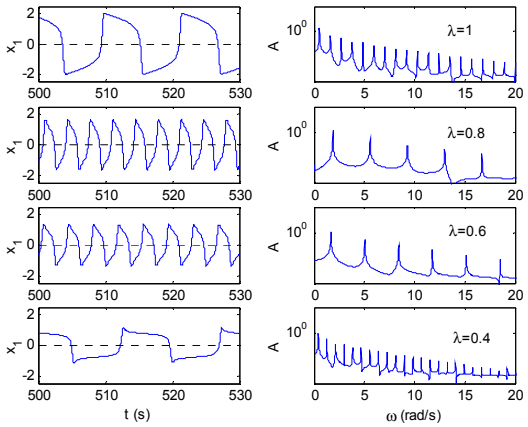

Figure 4 - time responses and Fourier spectra for $\lambda = \{1, 0.8, 0.6, 0.4\}$ and $\alpha = 5$.

3. Fractional order complex dynamics and control of legged robots

Walking machines allow locomotion in terrain inaccessible to other type of vehicles, since they do not need a continuous support surface, but at the cost of higher requirements for leg coordination and control. For these robots, joint level control is usually implemented through a PID like scheme. The application of the theory of fractional calculus in robotics joint control is still in a research stage, but the recent progress in this area reveals promising aspects for future developments [9].

In this line of thought, the first part of this study evaluates foot-ground interaction during the robot locomotion, for several walking conditions, and analyzes its dynamics in the viewpoint of fractional calculus. The main interest of this study stems from previous works showing that fractional dynamics arise in systems with "mixed" characteristics, such as the cases of a liquid interaction with a porous wall, in biological systems where there is the growth of tumors in healthy tissues and in backlash systems with continuous-discrete interactions [10].

The system under analysis reveals a behavior of this kind, namely with multiple periodic collisions among the robot feet and the ground. We consider a hexapod walking system (Fig. 5) with $n = 6$ legs, equally distributed along both sides of the robot body, having each two rotational joints (*i.e.*, $j = \{1, 2\} \equiv \{\text{hip, knee}\}$) [11]. For example, at the beginning of the support phase of each foot, although not desirable, often the contact of the foot with the ground is established and lost several times before stabilizing.

Figure 5 presents the dynamic model for the hexapod body and foot-ground interaction. It is considered robot body compliance because walking animals have a spine that allows supporting the locomotion with improved stability. The robot body

ISBN: 978-972-99064-4-2

is divided in n identical segments (each with mass $M_b n^{-1}$) and a linear spring-damper system (with parameters defined so that the body behaviour is similar to the one expected to occur on an animal) is adopted to implement the intra-body compliance [11]. The contact of the i^{th} robot feet with the ground is modelled through a non-linear system [12], being the values for the parameters based on the studies of soil mechanics [12].

In order to obtain the transfer functions (TF) of the system (i.e., the robot and the environment), the frequency response of the locomotion system is computed numerically. For that purpose, small amplitude sinusoidal exciting signals $\boldsymbol{\delta p_d}(t)$ are superimposed, separately, on the frequency range under analysis, over the x and y feet desired Cartesian trajectories, according to the block diagram presented in Fig. 6.

The resulting feet reference trajectories are given by:

$$\mathbf{p_d}(t)+\boldsymbol{\delta p}(t)=\begin{bmatrix} x_{id}(t)+\delta x_{id}(t) \\ y_{id}(t)+\delta y_{id}(t) \end{bmatrix} \tag{7a}$$

$$\begin{aligned} &\mathbf{p_d}(t)+\boldsymbol{\delta p}(t)=\boldsymbol{\psi}\left[\boldsymbol{\theta_d}(t)+\boldsymbol{\delta\theta_d}(t)\right]\Rightarrow \\ &\Rightarrow \boldsymbol{\theta_d}(t)+\boldsymbol{\delta\theta_d}(t)=\boldsymbol{\psi}^{-1}\left[\mathbf{p_d}(t)+\boldsymbol{\delta p}(t)\right] \end{aligned} \tag{7b}$$

where $\mathbf{p_d}(t) + \boldsymbol{\delta p_d}(t)$ are the i^{th} feet desired Cartesian trajectories (relatively to their hip) perturbed with a sinusoidal signal of small amplitude and $\boldsymbol{\Theta_d}(t) + \boldsymbol{\delta\Theta_d}(t)$, are the corresponding perturbed joint trajectories. During the robot locomotion simulation, the perturbations propagate to the torques demanded to the robot leg joint actuators by the controller (resulting $\boldsymbol{\Gamma_C}(t) + \boldsymbol{\delta\Gamma_C}(t)$) and to the robot real feet trajectories (that become $\mathbf{p_F}(t) + \boldsymbol{\delta p}(t)$).

The system TFs are given by (j = 1, 2):

$$G_{xj}(s)=\frac{F\{\delta x_{1F}(t)\}}{F\{\delta\tau_{1jC}(t)\}} \tag{8a}$$

$$G_{yj}(s)=\frac{F\{\delta y_{1F}(t)\}}{F\{\delta\tau_{1jC}(t)\}} \tag{8b}$$

where $\delta x_{1F}(t)$ and $\delta y_{1F}(t)$ are the resulting leg 1 foot trajectory perturbations, $\tau_{11C}(t)$ and $\tau_{12C}(t)$ are the corresponding joint demanded torques perturbations and $F\{\}$ represents the Fourier Transform operator.

In a first phase we develop a set of simulations to analyze the TFs of the hexapod-environment system for two different velocities, namely V_F = 1.0 ms^{-1} and V_F = 2.0 ms^{-1}.

In order to determine G_{xj} and G_{yj} (j = 1,2), the locomotion is simulated while the robot is moving

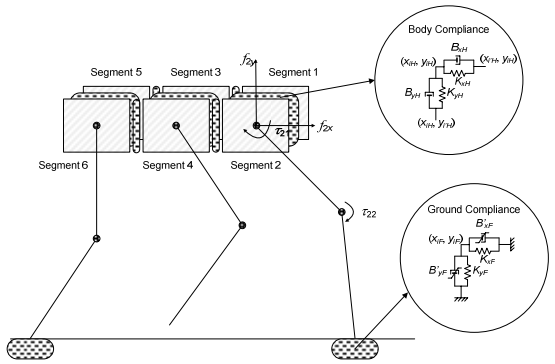

Figure 5 - model of the robot body and foot-ground interaction.

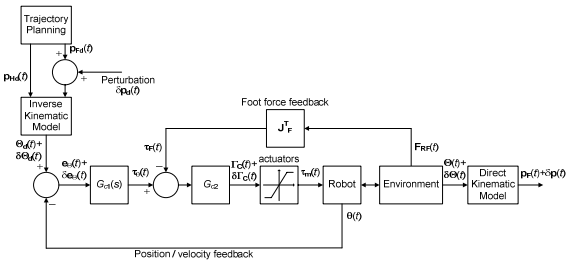

Figure 6 - block diagram adopted for the calculation of the transfer functions $G_{xj}(s)$ and $G_{yj}(s)$, j = 1,2.

on a perfectly flat surface without obstacles in its path. For this purpose, sinusoidal perturbations, with maximum amplitudes of $\delta x_{id}(t) = 10^{-4}$ m and $\delta y_{id}(t) = 10^{-4}$ m in the x and y directions, respectively, are superimposed, separately, over the planned robot feet Cartesian trajectories, in the range of frequencies 0.001 rads^{-1} $\leq \omega \leq$ 100.0 rads^{-1} during $Tsim \approx$ 40000 steps [10].

We start with G_{xj} for a robot forward locomotion speed of V_F = 1.0 ms^{-1}. As can be observed from the Nichols charts presented in Fig. 7, G_{x1} presents different asymptotes for different frequency ranges. At low frequencies (A ≡ [0.001; 0.05] rads^{-1}) the asymptote can be approximated by the expression:

$$G_{xj}(s)\approx\frac{k_{xj}}{j\left(s^{\alpha_{xj}+j\beta_{xj}}\right)},\ j=\sqrt{-1},\alpha_{xj},\beta_{xj}\in\Re,\ j=1,2 \tag{9}$$

The values of the parameters k_{xj}, α_{xj} and β_{xj} for the low frequency asymptotic approximation of G_{x1} are presented in Table 2.

At medium and at high frequencies (regions B ≡ [0.05; 0.5] rads^{-1} and C ≡ [0.5; 5.0] rads^{-1}), the resulting TFs can be approximated by an expression of the type:

$$G_{xj}(s)\approx\frac{k_{xj}}{s^{\alpha_{xj}+j\beta_{xj}}},\ \alpha_{xj},\beta_{xj}\in\Re,\ j=1,2 \tag{10}$$

The values of the parameters k_{xj}, α_{xj} and β_{xj} for the asymptotic approximations in these frequency ranges are also presented in Table 2.

ISBN: 978-972-99064-4-2

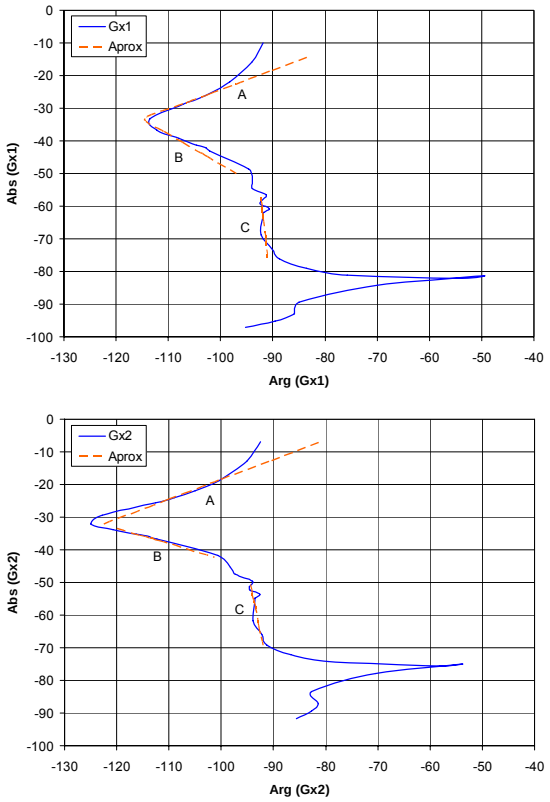

Figure 7 - Nichols charts of $G_{x1}(j\omega)$ and $G_{x2}(j\omega)$, and their approximations at low (A), medium (B) and high frequencies (C), for $V_F = 1.0$ ms^{-1}.

Table 2 - parameters values for the asymptotic approximations of the Nichols charts of G_{x1} and G_{x2}, with $V_F = 1.0$ ms^{-1}.

$V_F = 1.0$ ms^{-1}	G_{x1}			G_{x2}		
Frequency Range	k_{x1}	α_{x1}	β_{x1}	k_{x2}	α_{x2}	β_{x2}
Low (A)	0.001	0.72	0.18	0.001	0.77	0.22
Medium (B)	0.0014	0.84	-0.20	0.0022	1.03	-0.19
High (C)	0.00068	1.02	-0.01	0.002	1.04	-0.04

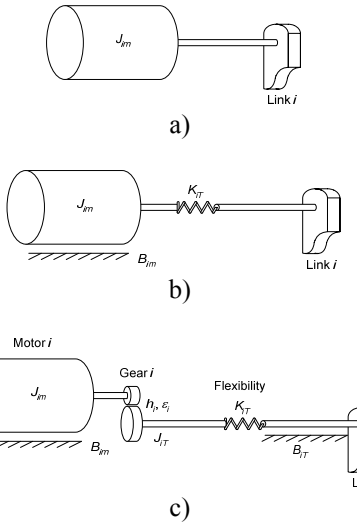

Figure 8 - model of the leg joint: *a)* ideal actuator and transmission, *b)* actuator with friction and transmission flexibility, and *c)* actuator and transmission with friction, flexibility and backlash.

These results reveal a complex order dynamics that is a consequence of the foot-ground interaction, with several free-impact-contact-impact-free dynamical states.

We verify that the Nichols chart of G_{x2} has similar features to those of G_{x1}, as can be observed in Fig. 7. The asymptotic approximations at low, medium and high frequencies, can be described by identical expressions and occur in the same frequency ranges as for the case of G_{x1}. The same can be concluded by comparing the values of the parameters α_{xj} and β_{xj}, for the asymptotic approximations of G_{x2} and G_{x1} (Table 2).

This study is repeated for a robot velocity of $V_F = 2.0$ ms^{-1} and the conclusions are identical.

The meaning of the imaginary factor j in the denominator of equation (9) in not yet clear. However, the authors believe on the existence of an expression unifying the asymptotic behavior of the TF both at low and medium frequencies, which is currently under investigation. One possibility, under study, is to replace the $s^{\alpha+j\beta}$, that leads to complex-valued outputs, by one of the operators $H_1(s) = s^{\alpha+j\beta} + s^{\alpha-j\beta}$ or $H_2(s) = j[s^{\alpha+j\beta} - s^{\alpha-j\beta}]$ that lead to real valued outputs. Supporting this consideration we have the similarities between the values of the parameters α_{xj} and β_{xj} (i.e., complex conjugate exponents for regions A and B) for the low and medium fre-quency asymptotic approximations of G_{xj} ($j = 1, 2$).

Knowing that fractional order controllers give better results than integer order ones when controlling systems that present fractional dynamics, and based on the previous results, the second part of this study compares two different robot controllers, namely an integer order Proportional and Derivative (PD) and a Fractional Order PD (PD$^{\alpha}$), in the presence of joints with viscous friction, flexibility and backlash.

In a first phase, we consider that the joint actuators and transmissions are ideal, as presented in Fig. 8a. Afterwards, in a second phase, we consider that the joint transmissions are non ideal, exhibiting a compliant behaviour (Fig. 8b). Finally, in a third phase we consider that the joint transmissions also include backlash (Fig. 8c), which causes the occurrence of impacts at the gear. These collisions obey the principle of conservation of Momentum, and the Newton's law.

The general control architecture of the hexapod robot is presented in Fig. 9 [13]. In this study we evaluate the effect of different PD$^{\alpha}$, $\alpha \in \Re$, controller implementations for $G_{c1}(s)$, while G_{c2} is a proportional controller with gain $Kp_j = 0.9$ ($j = 1, 2$). For the PD$^{\alpha}$ algorithm, implemented through a discrete-time 4th-order Padé approximation (a_{ij}, $b_{ij} \in \Re$, $j = 1, 2$), we have:

ISBN: 978-972-99064-4-2

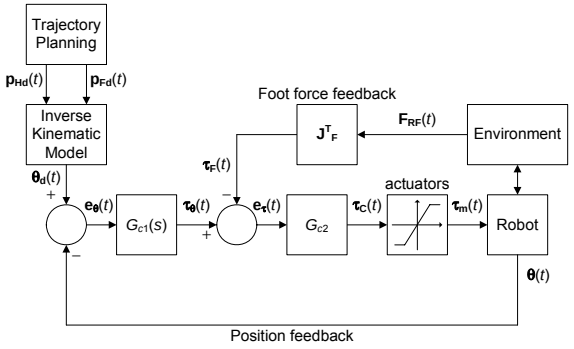

Figure 9 - hexapod robot control architecture.

$$G_{c1j}(z) \approx Kp_j + K\alpha_j \sum_{i=0}^{i=u} a_{ij}\, z^{-i} \Big/ \sum_{i=0}^{i=u} b_{ij}\, z^{-i} \qquad (11)$$

where Kp_j and $K\alpha_j$ are the proportional and derivative gains, respectively, and α_j is the fractional order, for joint j (in this case α_j = 0.5). Therefore, the classical (integer order) PD algorithm occurs when the fractional order α_j = 1.0.

The analysis is based on the formulation of two indices measuring the mean absolute density of energy per traveled distance (E_{av}) and the hip trajectory errors (ε_{xyH}) during walking, according to:

$$E_{av} = \frac{1}{d}\sum_{i=1}^{n}\sum_{j=1}^{m}\int_0^T \left|\boldsymbol{\tau}_{ij}(t)\,\dot{\boldsymbol{\theta}}_{ij}(t)\right| dt \quad \left[\mathrm{Jm}^{-1}\right] \qquad (12a)$$

$$\varepsilon_{xyH} = \sum_{i=1}^{n}\sqrt{\frac{1}{N_s}\sum_{k=1}^{N_s}\left(\Delta_{ixH}{}^2 + \Delta_{iyH}{}^2\right)} \quad [\mathrm{m}] \qquad (12b)$$

$$\Delta_{ixH} = x_{iHd}(k) - x_{iH}(k),\ \Delta_{iyH} = y_{iHd}(k) - y_{iH}(k)$$

To tune the controller we adopt a systematic method, testing and evaluating several possible combinations of parameters, for all controller implementations. In order to make a proper comparison of both controllers, we adopt the $G_{c1}(s)$ parameters that establish a compromise in what concerns the simultaneous minimisation of ε_{xyH} and E_{av}, on which the PD and the PD$^{\alpha}$ controllers present similar values for the indices ε_{xyH} and E_{av} and the motor torques and hip errors are also almost identical. Moreover, it is assumed high performance joint actuators, with a maximum actuator torque of τ_{ijMax} = 400 Nm.

With these controller settings, we analyse the system performance for the three different dynamical effects on the leg joints. Therefore, we start by considering an ideal joint transmission and, afterwards, we augment the model by including viscous friction, flexibility and backlash. The performance of both controllers is evaluated for the three cases, from the viewpoint of the proposed indices, while considering different levels of actuator saturation.

For the ideal transmission, the index E_{av} presents no significant variation for moderate saturation levels (*e.g.*, τ_{ijMax} > 120 Nm) being the performance of both controllers approximately similar. In the case of strong actuator saturation (*e.g.*, τ_{ijMax} < 100 Nm) the index reveals a large degradation with difficulties both for the PD and the PD$^{\alpha}$ algorithms.

Nevertheless, this situation is not realistic since it corresponds to operating conditions requiring joint torques much higher than those established by the saturation level. On the other hand, as expected, the robot hips trajectories errors are higher the smaller the maximum actuator torque. When comparing this index, for both control algorithms, we conclude that the PD controller presents smaller values of the index ε_{xyH} , for the entire range of variation of τ_{ijMax}.

The second situation consists of actuator model with viscous friction and joint transmission with flexibility. For this case the PD$^{\alpha}$ controller presents the lower values for the two indices (along most of the range of variation of K_{ijT} that keeps the robot locomotion stable) being the effect more noticeable the smaller the values of τ_{ijMax}.

On a third set of experiments we consider that the joint transmission model includes viscous friction, flexibility and backlash. For this case, the PD$^{\alpha}$ controller presents also lower values for the performance indices $\{E_{av},\ \varepsilon_{xyH}\}$ than the PD controller. This effect is more pronounced for smaller values of τ_{ijMax} and is visible on a large range of variation of the flexibility K_{ijT}, that keep the robot locomotion stable.

The same conclusion is valid for the entire range of variation of the restitution coefficient ε_{ij} and on a large range of variation of the backlash width h_{ij} (Fig.s 10 – 11).

From the above experiments we can conclude that the PD$^{\alpha}$ controller presents superior results when we have actuator saturation and dynamical phenomena on the joints. This means that, although tuned for identical performance in an ideal situation, the PD$^{\alpha}$ algorithm is more robust in a real operating condition.

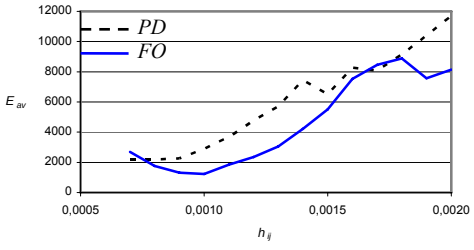

Figure 10 - E_{av} *vs.* h_{ij} for the PD and PD$^{\alpha}$ controllers, with τ_{ijMax} = 100 Nm.

ISBN: 978-972-99064-4-2

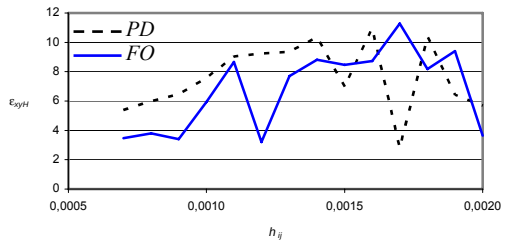

Figure 11 - ε_{xyH} *vs.* h_{ij} for the PD and PD$^{\alpha}$ controllers, with τ_{ijMax} = 100 Nm.

4. Fractional dynamics in the trajectory control of redundant manipulators

A kinematically redundant manipulator is a robotic arm possessing more degrees of freedom (*dof*) than those required to establish an arbitrary position and orientation of the gripper. Redundant manipulators offer several potential advantages over non-redundant arms. In a workspace with obstacles, the extra degrees of freedom can be used to move around or between obstacles and thereby to manipulate in situations that otherwise would be inaccessible [14-17].

When a manipulator is redundant, it is anticipated that the inverse kinematics admits an infinite number of solutions. This implies that, for a given location of the manipulator's gripper, it is possible to induce a self-motion of the structure without changing the location of the end effecter. Therefore, the arm can be reconfigured to find better postures for an assigned set of task requirements.

Several kinematic techniques for redundant manipulators control the gripper through the rates at which the joints are driven, using the pseudoinverse of the Jacobian [16, 19]. Nevertheless, these algorithms lead to a kind of chaotic motion with unpredictable arm configurations.

Having these ideas in mind, sub-section 4.1 introduces the fundamental issues for the kinematics of redundant manipulators. Based on these concepts, sub-section 4.2 presents the trajectory control of a three *dof* robot. The results reveal a chaotic behavior that is further analyzed in sub-section 4.3.

4.1 Kinematics of redundant manipulators

A kinematically redundant manipulator is a robotic arm possessing more *dof* than those required to establish an arbitrary position and orientation of the gripper. In Fig. 12 is depicted a planar manipulator with $k \in \aleph$ rotational (R) joints that is redundant for $k > 2$. When a manipulator is redundant it is anticipated that the inverse kinematics admits an infinite number of solutions. This implies that, for a given location of the manipulator's gripper, it is possible to induce a self-motion of the structure without changing the location of the gripper. Therefore, redundant manipulators can be reconfigured to find better postures for an assigned set of task requirements but, on the other hand, have a more complex structure requiring adequate control algorithms.

We consider a manipulator with n degrees of freedom whose joint variables are denoted by $\mathbf{q} = [q_1, q_2, ..., q_n]^T$. We assume that a class of tasks we are interested in can be described by m variables, $\mathbf{x} = [x_1, x_2, ..., x_m]^T$ ($m < n$) and that the relation between $\mathbf{q}$ and $\mathbf{x}$ is given by:

$$\mathbf{x} = f(\mathbf{q}) \tag{13}$$

where f is a function representing the direct kinematics.

Differentiating equation (13) with respect to time yields:

$$\dot{\mathbf{x}} = \mathbf{J}(\mathbf{q})\dot{\mathbf{q}} \tag{14}$$

where $\dot{\mathbf{x}} \in \Re^m$, $\dot{\mathbf{q}} \in \Re^n$ and $\mathbf{J}(\mathbf{q}) = \partial f(\mathbf{q}) / \partial \mathbf{q} \in \Re^{m \times n}$. Hence, it is possible to calculate a path $\mathbf{q}(t)$ in terms of a prescribed trajectory $\mathbf{x}(t)$ in the operational space. We assume that the following condition is satisfied:

$$\max \text{ rank } \{\mathbf{J}(\mathbf{q})\} = m \tag{15}$$

Failing to satisfy this condition usually means that the selection of manipulation variables is redundant and the number of these variables m can be reduced. When condition (14) is verified, we say that the degree of redundancy of the manipulator is $n-m$. If, for some $\mathbf{q}$ we have:

$$\text{rank } \{\mathbf{J}(\mathbf{q})\} < m \tag{16}$$

then the manipulator is in a singular state. This state is not desirable because, in this region of the trajectory, the manipulating ability is very limited.

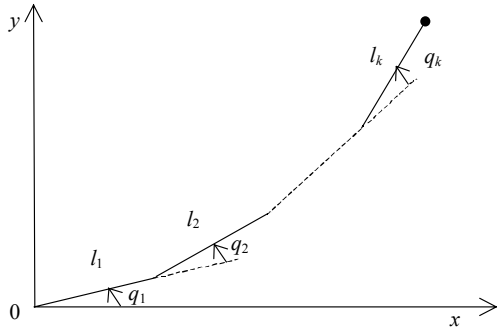

Figure 12 - a planar redundant planar manipulator with k rotational joints.

ISBN: 978-972-99064-4-2

Many approaches for solving redundancy [18, 21] are based on the inversion of equation (14). A solution in terms of the joint velocities is sought as:

$$\dot{\mathbf{q}} = \mathbf{J}^{\#}(\mathbf{q})\dot{\mathbf{x}} \tag{17}$$

where $\mathbf{J}^{\#}$ is one of the generalized inverses of the $\mathbf{J}$ [20-22]. It can be easily shown that a more general solution to equation (14) is given by:

$$\dot{\mathbf{q}} = \mathbf{J}^{+}(\mathbf{q})\dot{\mathbf{x}} + \left[\mathbf{I} - \mathbf{J}^{+}(\mathbf{q})\mathbf{J}(\mathbf{q})\right]\dot{\mathbf{q}}_0 \tag{18}$$

where $\mathbf{I}$ is the $n \times n$ identity matrix and $\dot{\mathbf{q}}_0 \in \Re^n$ is a $n \times 1$ arbitrary joint velocity vector and $\mathbf{J}^{+}$ is the pseudoinverse of the $\mathbf{J}$. The solution (18) is composed of two terms. The first term is relative to minimum norm joint velocities. The second term, the *homogeneous solution*, attempts to satisfy the additional constraints specified by $\dot{\mathbf{q}}_0$. Moreover, the matrix $\mathbf{I} - \mathbf{J}^{+}(\mathbf{q})\mathbf{J}(\mathbf{q})$ allows the projection of $\dot{\mathbf{q}}_0$ in the null space of $\mathbf{J}$. A direct consequence is that it is possible to generate internal motions that reconfigure the manipulator structure without changing the gripper position and orientation [21-24]. Another aspect revealed by the solution of equation (17) is that repetitive trajectories in the operational space do not lead to periodic trajectories in the joint space. This is an obstacle for the solution of many tasks because the resultant robot configurations have similarities with those of a chaotic system.

4.2 Robot trajectory control

The direct kinematics and the Jacobian of a 3-link planar manipulator with rotational joints (3*R* robot) has a simple recursive nature according with the expressions:

$$\begin{bmatrix} x \\ y \end{bmatrix} = \begin{bmatrix} l_1C_1 + l_2C_{12} + l_3C_{123} \\ l_1S_1 + l_2S_{12} + l_3S_{123} \end{bmatrix} \tag{19a}$$

$$\mathbf{J} = \begin{bmatrix} -l_1S_1 - \ldots - l_3S_{123} & \ldots & -l_3S_{123} \\ l_1C_1 + \ldots + l_3C_{123} & \ldots & l_3C_{123} \end{bmatrix} \tag{19b}$$

where l_i is the length of link i, $q_{i\ldots k} = q_i + \ldots + q_k$, $S_{i\ldots k} = Sin(q_{i\ldots k})$ and $C_{i\ldots k} = Cos(q_{i\ldots k})$.

During all the experiments it is considered $\Delta t = 10^{-3}$ sec, $L_{TOT} = l_1 + l_2 + l_3 = 3$ and $l_1 = l_2 = l_3$.

In the closed-loop pseudoinverse's method the joint positions can be computed through the time integration of the velocities according with the block diagram of the inverse kinematics algorithm depicted in Fig. 13 where $\mathbf{x}_{\mathbf{ref}}$ represents the vector of reference coordinates of the robot gripper in the operational space.

Based on equation (19) we analyze the kinematic performances of the 3*R*-robot when repeating a circular motion in the operational space with frequency $\omega_0 = 7.0$ rad sec^{-1}, centre at distance $r = [x^2+y^2]^{1/2}$ and radius ρ.

Figure 14 show the joint positions for the inverse kinematic algorithm (17) for r = {0.6, 2.0} and ρ = {0.3, 0.5}. We observe that:
- For r = 0.6 occur unpredictable motions with severe variations that lead to high joint transients [25]. Moreover, we verify a low frequency signal modulation that depends on the circle being executed.
- For r = 2.0 the motion is periodic with frequency identical to ω_0 = 7.0 rad sec^{-1}.

4.3 Analysis of the robot trajectories

In the previous section we verified that the pseudoinverse based algorithm leads to unpredictable arm configurations. In order to gain further insight into the pseudoinverse nature several distinct experiments are devised in the sequel during a time window of 300 cycles. Therefore, in a first set of experiments we calculate the Fourier transform of the 3*R*-robot joints velocities for a circular repetitive motion with frequency ω_0 = 7.0 rad sec^{-1}, radius ρ = {0.1, 0.3, 0.5, 0.7} and radial distances $r \in]0, L_{TOT} - \rho[$.

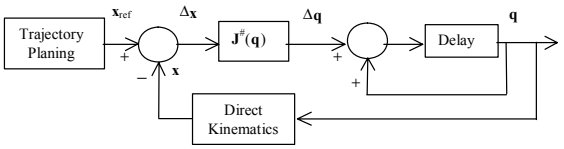

Figure 13 - block diagram of the closed-loop inverse kinematics algorithm with the pseudoinverse.

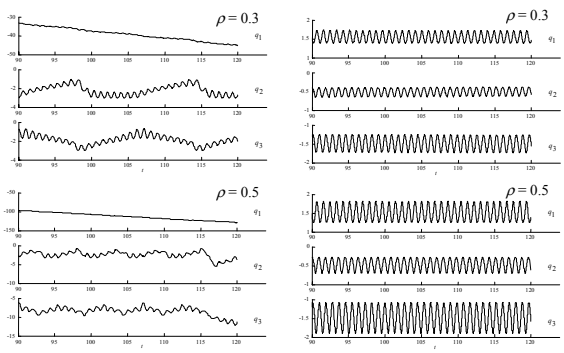

Figure 14 - the 3*R*-robot joint positions *versus* time using the pseudoinverse method for r = {0.6, 2.0} and ρ = {0.3, 0.5}.

ISBN: 978-972-99064-4-2

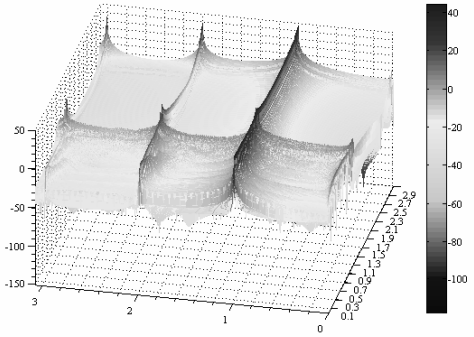

Figure 15 - $\left|F\left\{\dot{q}_2(t)\right\}\right|$ of the 3*R*-robot during 300 cycles, vs *r* and ω/ω_0, for $\rho = 0.1$, ω_0 = 7.0 rad sec^{-1}.

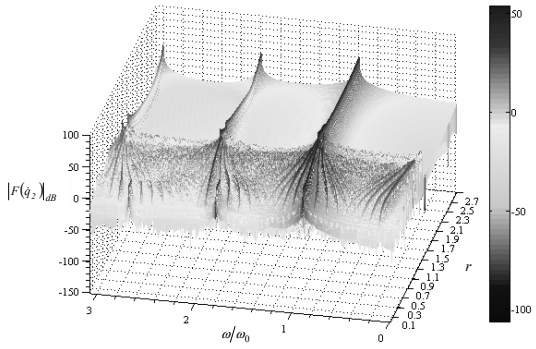

Figure 16 - $\left|F\left\{\dot{q}_2(t)\right\}\right|$ of the 3*R*-robot during 300 cycles, vs *r* and ω/ω_0, for $\rho = 0.3$, ω_0 = 7.0 rad sec^{-1}.

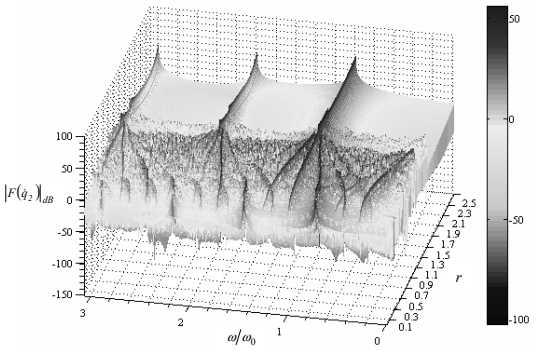

Figure 17 - $\left|F\left\{\dot{q}_2(t)\right\}\right|$ of the 3*R*-robot during 300 cycles, vs *r* and ω/ω_0, for $\rho = 0.5$, ω_0 = 7.0 rad sec^{-1}.

Figures 15 – 18 show $\left|F\left\{\dot{q}_2(t)\right\}\right|$ *versus* the frequency ratio ω_0/ω and the distance *r* where $F\{\ \}$ represents the Fourier operator. Is verified an interesting phenomenon induced by the gripper repetitive motion ω_0 because a large part of the energy is distributed along several sub-harmonics. These fractional order harmonics (*foh*) depend on *r*

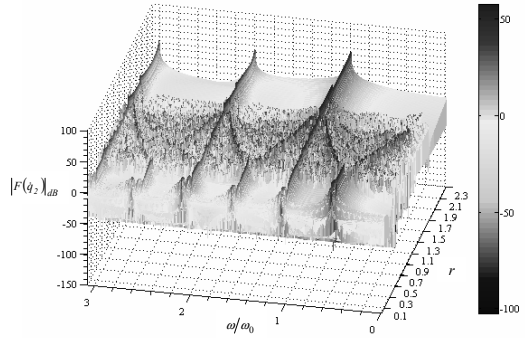

Figure 18 - $\left|F\left\{\dot{q}_2(t)\right\}\right|$ of the 3*R*-robot during 300 cycles, vs *r* and ω/ω_0, for $\rho = 0.7$, ω_0 = 7.0 rad sec^{-1}.

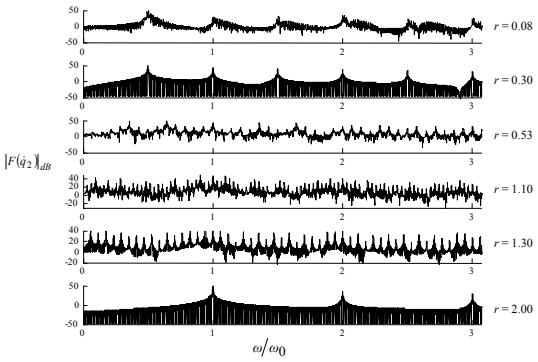

Figure 19 - $\left|F\left\{\dot{q}_2(t)\right\}\right|$ of the 3*R*-robot during 300 cycles, vs the frequency ratio ω/ω_0, for *r* = {0.08, 0.30, 0.53, 1.10, 1.30, 2.00}, $\rho = 0.7$, $\omega_0 = 7.0$ rad sec^{-1}.

and ρ making a complex pattern with similarities with those revealed by chaotic systems. Furthermore, we observe the existence of several distinct regions depending on *r*.

For example, selecting in Fig. 18 several distinct cases, namely for *r* = {0.08, 0.30, 0.53, 1.10, 1.30, 2.00}, we have the different signal Fourier spectra clearly visible in Fig. 19. Joints 1 and 3 show similar velocity spectra.

In the author's best knowledge the *foh* are aspects of fractional dynamics [26-28], but a final and assertive conclusion about a physical interpretation is a matter still to be explored.

For joints velocities 1 and 3 the results are similar to the verified ones for joint velocity 2.

5. Fractional order Fourier spectra in robotic manipulators with vibrations

This section presents a FC perspective in the study

ISBN: 978-972-99064-4-2

of the robotic signals captured during an impact phase of the manipulator. In the experiment is used a steel rod flexible link. To test impacts, the link consists on a long, thin, round, flexible steel rod clamped to the end-effector of the manipulator. The robot motion is programmed in a way such that the rod moves against a rigid surface. During the motion of the manipulator the clamped rod is moved by the robot against a rigid surface. An impact occurs and several signals are recorded with a sampling frequency of $f_s = 500$ Hz. In order to analyze the vibration and impact phenomena an acquisition system was developed [29]. The instrumentation system acquires signals from multiple sensors that capture the axis positions, mass accelerations, forces and moments and electrical currents in the motors. Afterwards, an analysis package, running off-line, reads the data recorded by the acquisition system and examines them.

Due to space limitations only some of the signals are depicted. A typical time evolution of the electrical currents of robot axis motors is shown in Fig. 20 corresponding to: (*i*) the impact of the rod on a rigid surface and (*ii*) without impact [30]. In this example, the signals present clearly a strong variation at the instant of the impact that occurs, approximately, at $t = 4$ sec.

In order to study the behavior of the signal Fourier transform, a trendline can be superimposed over the spectrum based on a power law approximation:

$$\left|\mathrm{F}\{f(t)\}\right| \approx c\omega^m \qquad (20)$$

where F{} is Fourier operator, c is a constant, ω is the frequency and m is the slope.

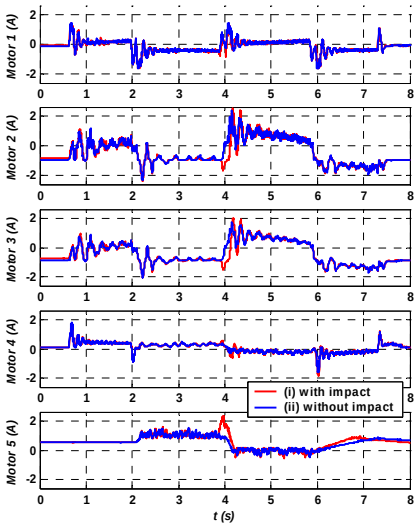

Figure 20 - electrical currents of robot axis motors.

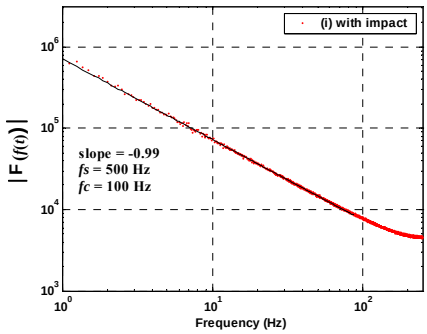

Figure 21 - spectrum of the axis 1 position.

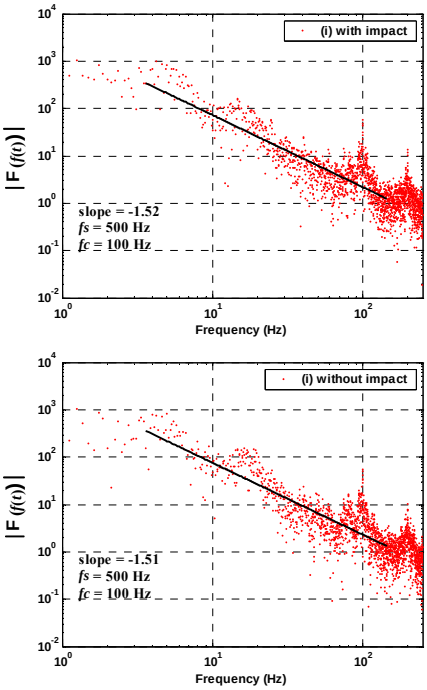

Figure 22 - spectrum of the axis 3 motor current.

Figure 21 shows the amplitude of the Fast Fourier Transform (FFT) of the axis 1 position signal. The trendline (20) leads to a slope $m = -0.99$ revealing, clearly, the integer order behavior. The others position signals were studied, revealing also an integer behavior, both under impact and no impact conditions.

Figure 22 shows the amplitude of the FFT of the electrical current for the axis 3 motor. The spectrum was also approximated by trendlines in a frequency range larger than one decade. These trendlines (Fig. 22) have slopes of $m = -1.52$ and $m = -1.51$ under impact (*i*) and without impact (*ii*) conditions, respectively. The lines present a fractional order behavior in both cases. The others axis motor currents were studied, as well. Some of them, for a limited frequency range, present also fractional order behavior while others have a complicated spectrum difficult to approximate by one trendline.

ISBN: 978-972-99064-4-2

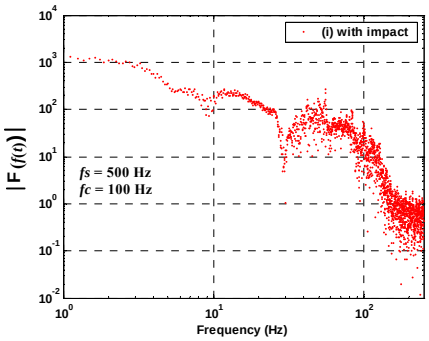

Figure 23 - F_z force spectrum with impact.

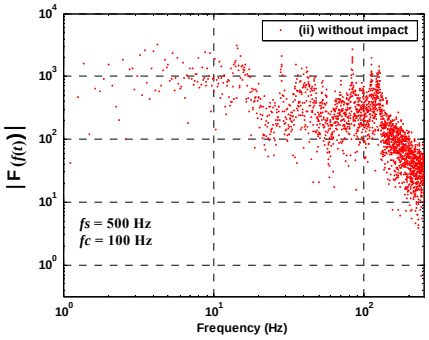

Figure 24 - acceleration spectrum of the rod free-end without impact.

Figure 23 shows, as example, the spectrum of the F_z force. This spectrum is not so well defined in a large frequency range. All force/moments spectra present identical behavior and, therefore, it is difficult to define accurately the behavior of the signals.

Finally, Fig. 24 depicts the spectrum of the signal captured from the accelerometer 1 located at the rod free-end of the beam. Like the spectrum from the other accelerometer located at the rod clamped-end, this spectrum is spread and complicated. Therefore, it is difficult to define accurately the slope of the signal and consequently its behavior in terms of integer or fractional system.

As shown in the examples, the Fourier spectrum of several signals, captured during an impact phase of the manipulator, presents a non integer behavior. On the other hand, the feedback fractional order systems, due to the success in the synthesis of real noninteger differentiator and the emergence of fractional-order controllers, have been designed and applied to control a variety of dynamical processes [31]. Therefore the study presented here can assist in the design of the control system to be used in reducing or eliminating the effect of vibrations.

6. Manipulator position/force control

Raibert and Craig [32] introduced the concept of force control based on the hybrid algorithm and, since then, several researchers developed those ideas and proposed other schemes [33].

There are two basic methods for force control, namely the hybrid position/ force and the impedance schemes. The first method separates the task into two orthogonal sub-spaces corresponding to the force and the position controlled variables. Once established the subspace decomposition two independent controllers are designed. The second method [33] requires the definition of the arm mechanical impedance. The impedance accommodates the interaction forces that can be controlled to obtain an adequate response.

The dynamical equation of a n dof robot is:

$$\boldsymbol{\tau} = \mathbf{H}(\mathbf{q})\ddot{\mathbf{q}} + \mathbf{C}(\mathbf{q},\dot{\mathbf{q}}) + \mathbf{G}(\mathbf{q}) - \mathbf{J}^{\mathrm{T}}(\mathbf{q})\mathbf{F} \qquad (21)$$

where $\boldsymbol{\tau}$ is the $n \times 1$ vector of actuator torques, $\mathbf{q}$ is the $n \times 1$ vector of joint coordinates, $\mathbf{H}(\mathbf{q})$ is the $n \times n$ inertia matrix, $\mathbf{C}(\mathbf{q},\dot{\mathbf{q}})$ is the $n \times 1$ vector of centrifugal/Coriolis terms and $\mathbf{G}(\mathbf{q})$ is the $n \times 1$ vector of gravitational effects. The $n \times m$ matrix $\mathbf{J}^{\mathrm{T}}(\mathbf{q})$ is the transpose of the Jacobian matrix of the robot and $\mathbf{F}$ is the $m \times 1$ vector of the force that the (m-dimensional) environment exerts in the robot gripper.

$$\mathbf{H}(\mathbf{q}) = \begin{bmatrix} (m_1+m_2)r_1^2 + m_2 r_2^2 + \\ 2m_2 r_1 r_2 C_2 + J_{1m} + J_{1g} & \begin{matrix} m_2 r_2^2 + \\ m_2 r_1 r_2 C_2 \end{matrix} \\ \hline m_2 r_2^2 + m_2 r_1 r_2 C_2 & \begin{matrix} m_2 r_2^2 + \\ J_{2m} + J_{2g} \end{matrix} \end{bmatrix} \qquad (22a)$$

$$\mathbf{C}(\mathbf{q},\dot{\mathbf{q}}) = \begin{bmatrix} -m_2 r_1 r_2 S_2 \dot{q}_2^{\,2} - 2m_2 r_1 r_2 S_2 \dot{q}_1 \dot{q}_2 \\ m_2 r_1 r_2 S_2 \dot{q}_1^{\,2} \end{bmatrix} \qquad (22b)$$

$$\mathbf{G}(\mathbf{q}) = \begin{bmatrix} g(m_1 r_1 C_1 + m_2 r_1 C_1 + m_2 r_2 C_{12}) \\ g m_2 r_2 C_{12} \end{bmatrix} \qquad (22c)$$

$$\mathbf{J}^{\mathrm{T}}(\mathbf{q}) = \begin{bmatrix} -r_1 S_1 - r_2 S_{12} & r_1 C_{11} + r_2 C_{12} \\ -r_2 S_{12} & r_2 C_{12} \end{bmatrix} \qquad (22d)$$

where $C_{ij} = \cos(q_i + q_j)$ and $S_{ij} = \sin(q_i + q_j)$.

The numerical values adopted for the 2R robot [34, 35] are $m_1 = 0.5$ kg, $m_2 = 6.25$ kg, $r_1 = 1.0$ m, $r_2 = 0.8$ m, $J_{1m} = J_{2m} = 1.0$ kgm^2 and $J_{1g} = J_{2g} = 4.0$ kgm^2.

The constraint plane is determined by the angle θ (Fig. 25) and the contact displacement x_c of the robot gripper with the constraint surface is modeled through a linear system with a mass M, a damping B and a stiffness K with dynamics:

$$F_c = M\ddot{x}_c + B\dot{x}_c + Kx_c \qquad (23)$$

In order to study the dynamics and control of one robot we adopt the position/force hybrid control with the implementation of the integer order and fractional-order algorithms [5, 6, 26, 36]. The

ISBN: 978-972-99064-4-2

system performance and robustness is analyzed in the time domain. The effect of dynamic backlash and flexibility is also investigated.

6.1 The hybrid controller

The structure of the position/force hybrid control algorithm is depicted in Fig. 26. The diagonal $n \times n$ selection matrix **S** has elements equal to one (zero) in the position (force) controlled directions and **I** is the $n \times n$ identity matrix. In this paper the y_c (x_c) cartesian coordinate is position (force) controlled, yielding:

$$\mathbf{S} = \begin{bmatrix} 0 & 0 \\ 0 & 1 \end{bmatrix} \tag{24a}$$

$$\mathbf{J_c}(\mathbf{q}) = \begin{bmatrix} -r_1 C_{\theta 11} - r_2 C_{\theta 12} & -r_2 C_{\theta 12} \\ r_1 S_{\theta 11} + r_2 S_{\theta 12} & r_2 S_{\theta 12} \end{bmatrix} \tag{24b}$$

where $C_{\theta ij} = \cos(\theta - q_i - q_j)$ and $S_{\theta ij} = \sin(\theta - q_i - q_j)$.

6.2 Controller performances

This section analyzes the system performance both for ideal transmissions and robots with dynamic phenomena at the joints, such as backlash and flexibility. Moreover, we compare the response of *FO* and the *PD*: $C_P(s) = K_p + K_d\, s$ and *PI*: $C_F(s) = K_p + K_i\, s^{-1}$ controllers, in the position and force loops.

Both algorithms were tuned by trial and error having in mind getting a similar performance in the two cases. The resulting parameters were *FO*: $\{K_P, \alpha_P\} \equiv \{10^5, 1/2\}$, $\{K_F, \alpha_F\} \equiv \{10^3, -1/5\}$ and *PD*/*PI*: $\{K_p, K_d\} \equiv \{10^4, 10^3\}$, $\{K_p, K_i\} \equiv \{10^3, 10^2\}$ for the position and force loops, respectively. Moreover, it is adopted the operating point $\{x, y\} \equiv \{1,1\}$, a constraint surface with parameters $\{\theta, M, B, K\} \equiv \{\pi/2, 10^3, 1.0, 10^2\}$ and a controller sampling frequency $f_c = 1$ kHz.

In order to study the system dynamics we apply, separately, rectangular pulses, at the position and force references, that is, we perturb the references with $\{\delta y_{cd}, \delta F_{cd}\} = \{10^{-1}, 0\}$ and $\{\delta y_{cd}, \delta F_{cd}\} = \{0, 10^{-1}\}$.

Figures 27 and 28 depict the time response of the 2*R* robot under the action of the *FO* and the *PD/PI* controllers for ideal transmissions at the joints.

In a second phase (Fig.s 29 and 30) we analyze the response of a 2*R* robot with dynamic backlash at the joints. For the *i*th joint gear, with clearance h_i, the backlash reveals impact phenomena between the inertias, which obey the principle of conservation of momentum and the Newton law:

$$\dot{q}_i' = \frac{\dot{q}_i (J_{ii} - \varepsilon J_{im}) + \dot{q}_{im} J_{im} (1 + \varepsilon)}{J_{ii} + J_{im}} \tag{25a}$$

$$\dot{q}_{im}' = \frac{\dot{q}_i J_i (1 + \varepsilon) + \dot{q}_{im} (J_{im} - \varepsilon J_{ii})}{J_{ii} + J_{im}} \tag{25b}$$

where $0 \le \varepsilon \le 1$ defines the type of impact ($\varepsilon = 0$ inelastic impact, $\varepsilon = 1$ elastic), $\dot{q}_i'$ and $\dot{q}_{im}'$ are the inertias velocities of the joint and motor after the collision, and t J_{ii} and J_{im} stand for the link and motor *i*th joint inertias. In the simulations is adopted $h_i = 1.8\ 10^{-4}$ rad and $\varepsilon_i = 0.8$ ($i = 1,2$).

In a third phase (Fig.s 31 and 32) it is studied the case of compliant joints, where the dynamic model corresponds to equation (21) augmented by the equations:

$$\boldsymbol{\tau} = \mathbf{J_m}\ddot{\mathbf{q}}_\mathbf{m} + \mathbf{B_m}\dot{\mathbf{q}}_\mathbf{m} + \mathbf{K_m}(\mathbf{q_m} - \mathbf{q}) \tag{26a}$$

$$\mathbf{K_m}(\mathbf{q_m} - \mathbf{q}) = \mathbf{J}(\mathbf{q})\ddot{\mathbf{q}} + \mathbf{C}(\mathbf{q}, \dot{\mathbf{q}}) + \mathbf{G}(\mathbf{q}) \tag{26b}$$

where $\mathbf{J_m}$, $\mathbf{B_m}$ and $\mathbf{K_m}$ are the $n \times n$ diagonal matrices of the motor and transmission inertias, damping and stiffness, respectively. In the simulations we adopt $K_{mi} = 2\ 10^6$ Nm rad^{-1} and $B_{mi} = 10^4$ Nms rad^{-1} ($i = 1,2$).

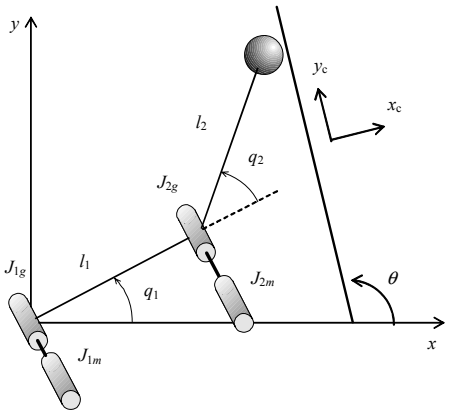

Figure 25 - the 2*R* robot and the constraint surface.

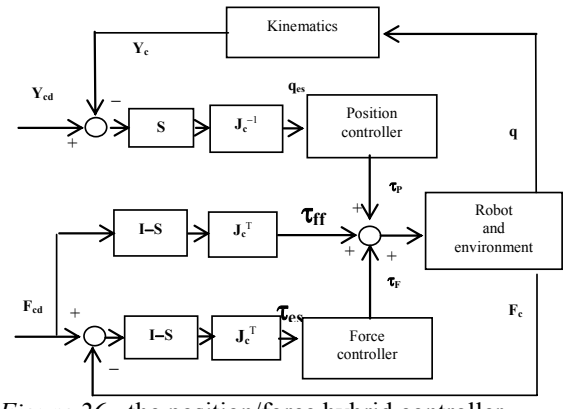

Figure 26 - the position/force hybrid controller.

The time responses (Tables 3 and 4), namely the percent overshoot *PO%*, the steady-state error e_{ss}, the peak time T_p and the settling time T_s, reveal that,

ISBN: 978-972-99064-4-2

although tuned for similar performances in the first case, the *FO* is superior to the *PD/PI* in the cases with dynamical phenomena at the robot joints.

7. Position/force control of two arms working in cooperation

Two robots carrying a common object are a logical alternative for the case in which a single robot is not able to handle the load. The choice of a robotic mechanism depends on the task or the type of work to be performed and, consequently, is determined by the position of the robots and by their dimensions and structure.

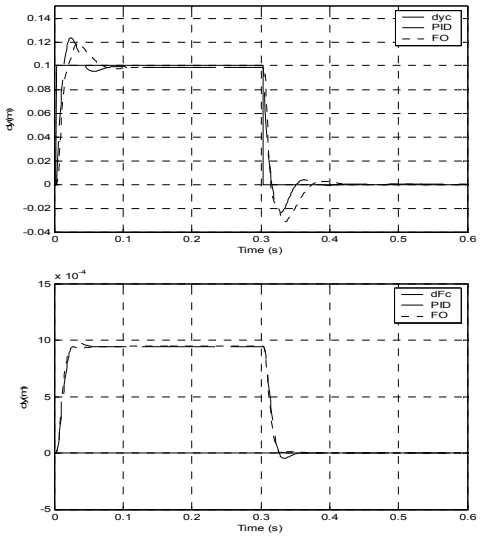

Figure 27 - time response for the 2*R* robot with ideal transmission at the joints under the action of the *FO* and *PD*/*PI* controllers for a pulse perturbation at the robot position reference.

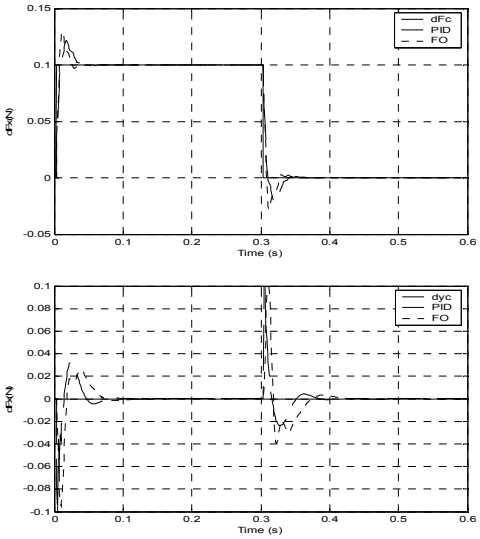

Figure 28 - time response for the 2*R* robot with ideal transmission at the joints under the action of the *FO* and *PD*/*PI* controllers for a pulse perturbation at the robot force reference.

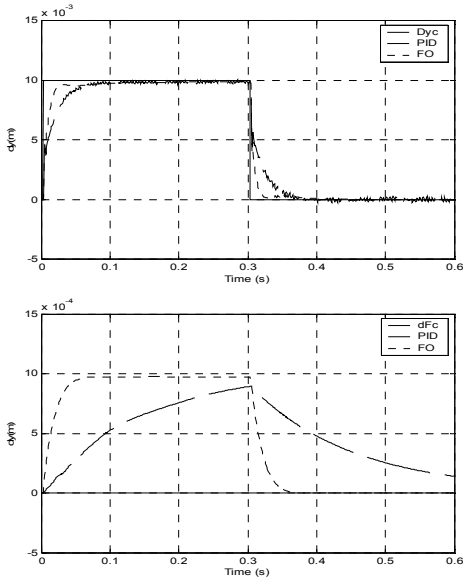

Figure 29 - time response for 2*R* robot with dynamic backlash at the joints under the action of the *FO* and *PD*/*PI* controllers for a pulse perturbation at the robot position reference.

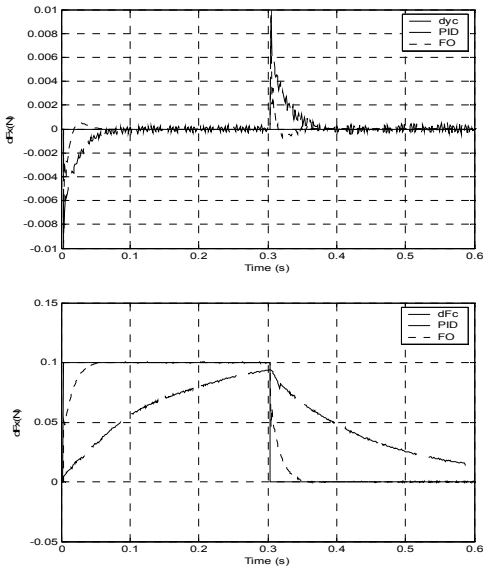

Figure 30 - time response for 2*R* robot with dynamic backlash at the joints under the action of the *FO* and *PD*/*PI* controllers for a pulse perturbation at the robot force reference.

In general, the selection is done through experience and intuition; nevertheless, it is important to measure the manipulation capability of the robotic system [37] that can be useful in the robot operation. In this perspective it was proposed the concept of kinematic manipulability [38] and its generalization by including the dynamics [39] or, alters natively, the statistical evaluation of manipulation [40]. Other related aspects such as the coordination of two robots handling objects, collision avoidance and free path planning have been also investigated [41]. With two cooperative robots the resulting interaction forces have to be accommodated and consequently,

ISBN: 978-972-99064-4-2

in addition to position feedback, force control is also required to accomplish adequate performances [42].

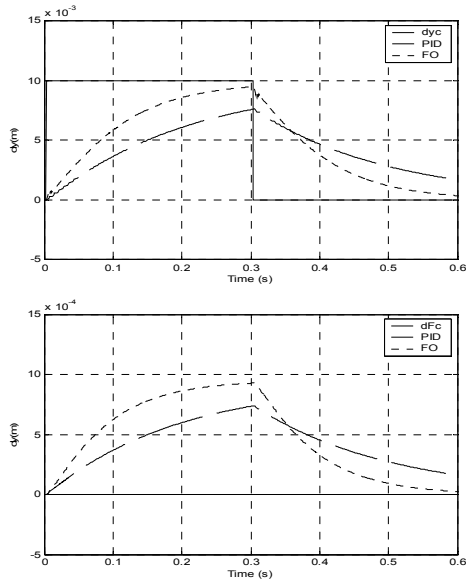

Figure 31 - time response for 2*R* robot with flexibility at the joints under the action of the *FO* and *PD*/*PI* controllers for a pulse perturbation at the robot position reference.

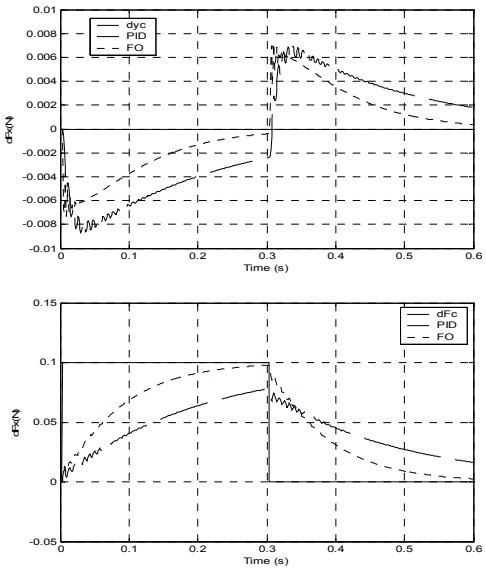

Figure 32 - time response for 2*R* robot with flexibility at the joints under the action of the *FO* and *PD*/*PI* controllers for a pulse perturbation at the robot force reference.

Table 3 - time response characteristics for a perturbation δy_{cd}.

joint		*PO%*	e_{ss}	T_p	T_s
ideal	*PID*	23.48%	$99\ 10^{-3}$	0.122	0.013
	FO	18.98%	$79\ 10^{-3}$	0.033	0.018
backlash	*PID*	0.37%	$2.1\ 10^{-3}$	0.383	0.080
	FO	0.36%	$1.4\ 10^{-4}$	0.302	0.118
flexible	*PID*	2.28%	$3.9\ 10^{-3}$	0.403	1.502
	FO	1.80%	$1.4\ 10^{-3}$	0.302	3.004

Table 4 - time response characteristics for a perturbation δF_{cd}.

joint		*PO%*	e_{ss}	T_p	T_s
ideal	*PID*	22.04%	$1.3\ 10^{-3}$	0.083	0.091
	FO	29.54%	$1.3\ 10^{-3}$	0.089	0.093
backlash	*PID*	5.98%	$9.9\ 10^{-2}$	0.402	0.405
	FO	0.86%	$9.9\ 10^{-2}$	0.079	0.043
flexible	*PID*	3.28%	$9.9\ 10^{-2}$	0.602	0.602
	FO	1.82%	$9.9\ 10^{-2}$	0.450	0.450

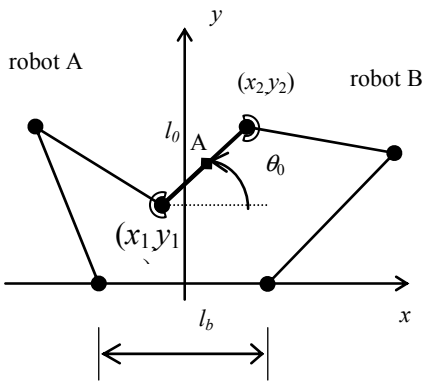

Figure 33 - the 2*R* dual arm robot and the constraint surface.

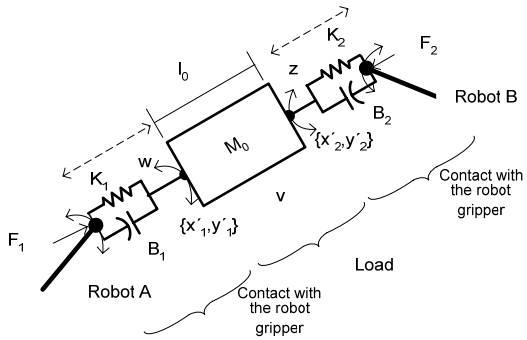

Figure 34 - the contact between the robot gripper and the object.

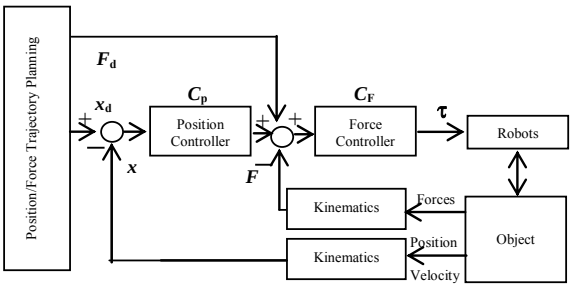

Figure 35 - the position/force cascade controller.

We consider two 2*R* cooperating manipulators with identical dimensions (Fig. 33). The contact of the robot gripper with the load is modeled through a linear system with a mass *M*, a damping *B* and a stiffness *K* (Fig. 34).

The controller architecture (Fig. 35) is inspired on the impedance and compliance schemes. Therefore, we establish a cascade of force and position

ISBN: 978-972-99064-4-2

algorithms as internal an external feedback loops, respectively, where $\mathbf{x_d}$ and $\mathbf{F_d}$ are the payload desired position coordinates and contact forces.

7.1 Controller performances

This section analyzes the system performance both for robots ideal transmissions and robots with dynamic phenomena at the joints, such as backlash and flexibility. Moreover, we compare the response of *FO* and classical algorithms namely *PD*: $C_P(s) = K_p\,(1 + T_d\,s)$ and *PI*: $C_F(s) = K_F\,[1 + (T_i\,s)^{-1}]$, in the position and force loops, respectively. Both algorithms were tuned by trial and error having in mind getting a similar performance in the two cases. The resulting parameters were *FO*: $\{K_P,\alpha_P\} \equiv \{10^4,\ 1/2\}$, $\{K_F,\alpha_F\} \equiv \{2,-1/5\}$ and *PD*/*PI*: $\{K_p,K_d\} \equiv \{10^4,10^2\}$, $\{K_p,K_i\} \equiv \{10,10^4\}$ for the position and force loops, respectively. Moreover, it is adopted the operating point, the center of the object A $\equiv \{x,y\} \equiv \{0,1\}$ and a object surface with parameters $\{\theta,M,B_j,K_j\} \equiv \{0,10,1.0,10^3\}$.

In order to study the system dynamics we apply, separately, small amplitude rectangular pulses, at the position and force references. Therefore, we perturb the references with $\delta x_d = 10^{-3}$, $\delta y_d = 10^{-3}$, $\delta Fx_d = 1.0$, $\delta Fy_d = 1.$ and we analyze the system performance in the time domain.

To evaluate the performance of the proposed algorithms we compare the response for robots with dynamical phenomena at the joints. In all experiments the controller sampling frequency is $f_c = 10$ kHz for the operating point A of the object and a contact force of each gripper of $\{Fx_j,Fy_j\} \equiv \{0.5,5\}$ *Nm* for the *j*th (j = 1, 2) robot.

Figure 36 depicts the time response of the robot A, under the action of the *FO* and the *PD/PI* algorithms, for robots with ideal transmissions at the joints.

In Fig.s 37 and 38 we analyze the response of robots with dynamic backlash and dynamic flexibility at the joints.

The time responses (Tables 5 – 8), namely the percent overshoot *PO%*, the steady-state error e_{ss}, the peak time T_p and the settling time T_s, reveal that, although tuned for similar performances in the first case, the *FO* is superior to the *PD/PI* in the cases with dynamical phenomena at the robot joints.

8. Heat diffusion

The heat diffusion is governed by a linear one-dimensional partial differential equation (PDE) of the form:

$$\frac{\partial u}{\partial t} = k\,\frac{\partial^2 u}{\partial x^2} \tag{27}$$

where k is the diffusivity, t is the time, u is the temperature and x is the space coordinate. The system (27) involves the solution of a PDE of parabolic type for which the standard theory guarantees the existence of a unique solution [44].

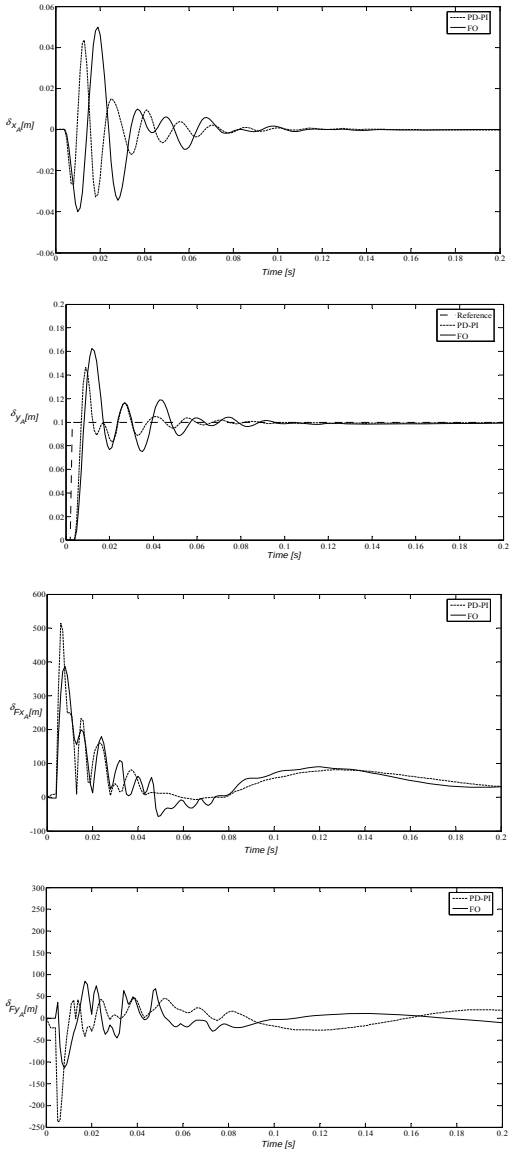

Figure 36 - time response of robots with ideal joints under the action of the *FO* and the *PD−PI* algorithms for a pulse perturbation at the robot A position reference $\delta y_d = 10^{-3}$ m and a payload M = 1 kg, B_i = 1 Ns/m and $K_i = 10^3$ N/m.

ISBN: 978-972-99064-4-2

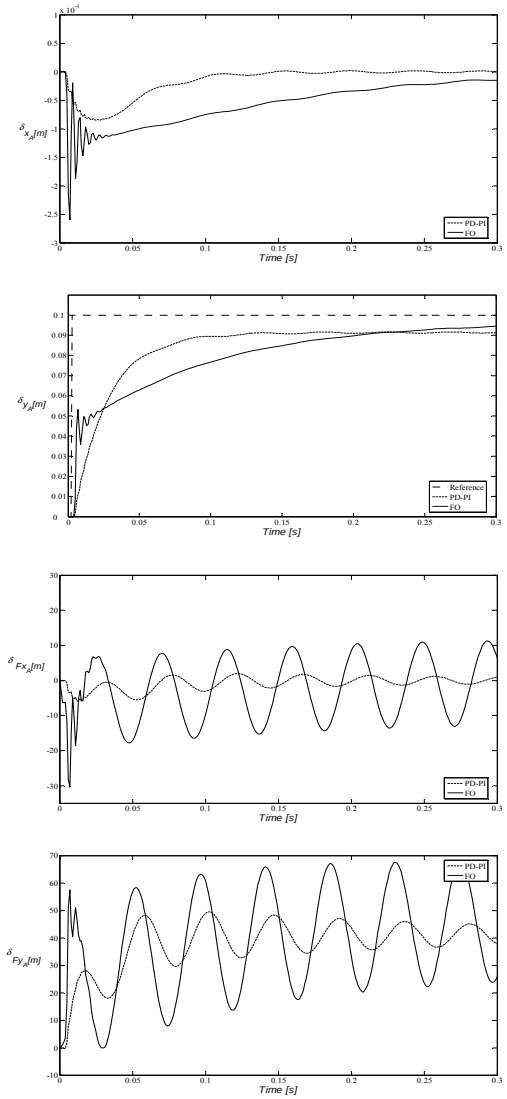

Figure 37 - time response of robots with joints having backlash under the action of the *FO* and the *PD−PI* algorithms, for a pulse perturbation at the robot A position reference $\delta y_d = 10^{-3}$ m and a payload $M = 1$ kg, $B_i = 1$ Ns/m and $K_i = 10^3$ N/m.

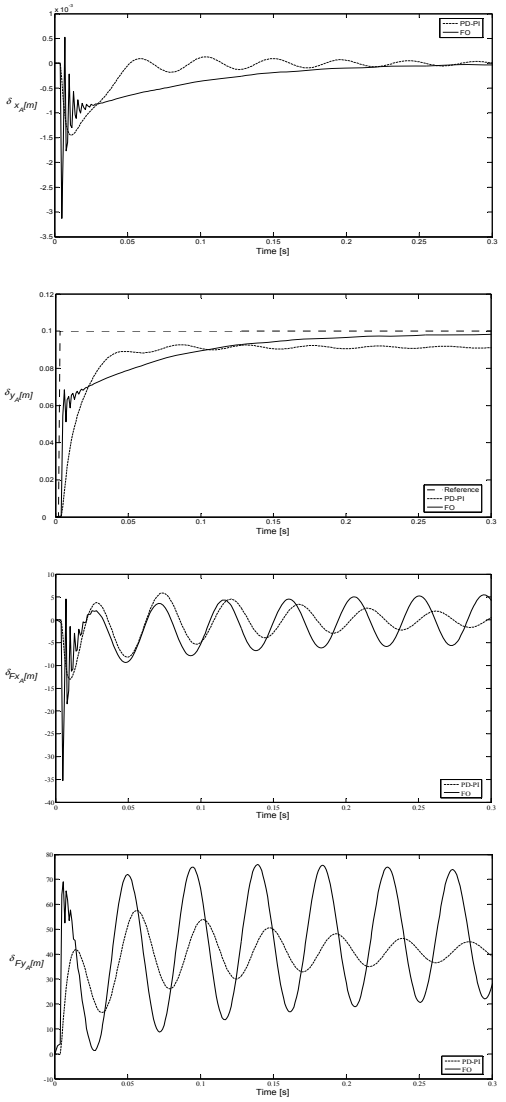

Figure 38 - time response of robots with joints having backlash under the action of the *FO* and the *PD−PI* algorithms, for a pulse perturbation at the robot A position reference $\delta y_d = 10^{-3}$ m and a payload $M = 1$ kg, $B_i = 1$ Ns/m and $K_i = 10^3$ N/m.

Table 5 - time response characteristics for a perturbation δx_d the robot A position reference.

Joint		*PO%*	e_{ss}	T_p	T_s
Ideal	*PID*	33.89	$9.8\ 10^{-4}$	$17\ 10^{-3}$	$70\ 10^{-2}$
	FO	25.39	$8.3\ 10^{-4}$	$9\ 10^{-3}$	$50\ 10^{-2}$
Backlash	*PID*	4.5	$5.3\ 10^{-3}$	$17\ 10^{-3}$	$31\ 10^{-3}$
	FO	1.05	$2.2\ 10^{-4}$	$13\ 10^{-3}$	$30\ 10^{-3}$
Flexible	*PID*	4.87	$10\ 10^{-2}$	$35\ 10^{-3}$	$71\ 10^{-3}$
	FO	2.51	$2.2\ 10^{-3}$	$33\ 10^{-3}$	$60\ 10^{-2}$

Table 6 - time response characteristics for a perturbation δy_d the robot A position reference.

Joint		*PO%*	e_{ss}	T_p	T_s
Ideal	*PID*	40.6	$9.7\ 10^{-4}$	$23\ 10^{-2}$	$70\ 10^{-2}$
	FO	25.87	$4.7\ 10^{-4}$	$9\ 10^{-1}$	$45\ 10^{-2}$
Backlash	*PID*	9.5	$9.6\ 10^{-3}$	$66\ 10^{-2}$	$91\ 10^{-2}$
	FO	9.7	$9.7\ 10^{-3}$	$80\ 10^{-3}$	$90\ 10^{-3}$
Flexible	*PID*	9.6	$9.7\ 10^{-3}$	$98\ 10^{-2}$	$98\ 10^{-2}$
	FO	8.8	$2.2\ 10^{-3}$	$93\ 10^{-3}$	$93\ 10^{-2}$

Table 7 - time response characteristics for a perturbation δFx_d at the robot A force reference.

Joint		*PO%*	e_{ss}	T_p	T_s
Ideal	*PID*	–78.54	$102\ 10^{-2}$	$11\ 10^{-3}$	$23\ 10^{-3}$
	FO	–90.32	$94\ 10^{-2}$	$99\ 10^{-3}$	$199\ 10^{-3}$
backlash	*PID*	–89.85	$93\ 10^{-2}$	$10\ 10^{-2}$	$20\ 10^{-2}$
	FO	–92.32	$93\ 10^{-2}$	$27\ 10^{-2}$	$55\ 10^{-2}$
Flexible	*PID*	–89.51	$94\ 10^{-2}$	$5.6\ 10^{-2}$	$11\ 10^{-2}$
	FO	–91.76	$93\ 10^{-2}$	$23\ 10^{-2}$	$47\ 10^{-2}$

Table 8 - time response characteristics for a perturbation δFy_d at the robot A force reference.

joint		*PO%*	e_{ss}	T_p	T_s
ideal	*PID*	–78.96	$10\ 10^{-1}$	$14\ 10^{-3}$	$29\ 10^{-3}$
	FO	–90.69	$9.4\ 10^{-2}$	$99\ 10^{-3}$	$199\ 10^{-3}$
backlash	*PID*	–90.63	$93\ 10^{-2}$	$23\ 10^{-2}$	$46\ 10^{-2}$
	FO	–92.01	$93\ 10^{-2}$	$72\ 10^{-2}$	$145\ 10^{-2}$
flexible	*PID*	–90.67	$93\ 10^{-2}$	$14\ 10^{-2}$	$29\ 10^{-2}$

ISBN: 978-972-99064-4-2

For the case of a planar perfectly isolated surface we usually apply a constant temperature U_0 at $x = 0$ and analyzes the heat diffusion along the horizontal coordinate x. Under these conditions, the heat diffusion phenomenon is described by a non-integer order model:

$$U(x,s)=\frac{U_0}{s}G(s) \quad G(s)=e^{-x\sqrt{\frac{s}{k}}} \tag{28}$$

where x is the space coordinate, U_0 is the boundary condition and $G(s)$ is the system transfer function.

In our study, the simulation of the heat diffusion is performed by adopting the Crank-Nicholson implicit numerical integration based on the discrete approximation to differentiation as [43-45]:

$$\begin{aligned}-ru[j+1,i+1]+(2+r)u[j+1,i]-ru[j+1,i-1]=\\ =ru[j,i+1]+(2-r)u[j,i]+u[j,i-1]\end{aligned} \tag{29}$$

where $r = k\Delta t(\Delta x^2)^{-1}$, $\{\Delta x, \Delta t\}$ and $\{i, j\}$ are the increments and the integration indices for space and time, respectively.

8.1 Control strategies

The generalized PID controller $G_c(s)$ has a transfer function of the form:

$$G_c(s)=K\left[1+\frac{1}{T_i s^{\alpha}}+T_d s^{\beta}\right] \tag{30}$$

where α and β are the orders of the fractional integrator and differentiator, respectively. The constants K, T_i and T_d are correspondingly the proportional gain, the integral time constant and the derivative time constant.

Clearly, taking $(\alpha, \beta) = \{(1, 1), (1, 0), (0, 1), (0, 0)\}$ we get the classical {PID, PI, PD, P} controllers, respectively.

The $PI^{\alpha}D^{\beta}$ controller is more flexible and gives the possibility of adjusting more carefully the closed-loop system characteristics.

In the next two sub-sections, we analyze the system of Fig. 39 by adopting the classical integer-order PID and a fractional PID^{β}, respectively.

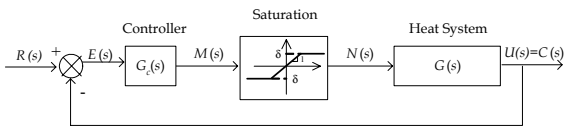

Figure 39 - closed-loop system with PID controller $G_c(s)$.

8.2 PID tuning using Ziegler-Nichols rule

In this sub-section we analyze the closed-loop system with a conventional PID controller given by the transfer function (30) with $\alpha = \beta = 1$. Usually, the PID parameters (K, T_i, T_d) are tuned by using the so-called Ziegler-Nichols open loop (ZNOL) method [45]. The ZNOL heuristics are based on the approximate first-order plus dead-time model:

$$\hat{G}(s)=\frac{K_p}{\tau s+1}e^{-sT} \tag{31}$$

For the heat system, the resulting parameters are $\{K_p, \tau, T\} = \{0.52, 162, 28\}$ leading to the PID constants $\{K, T_i, T_d\} = \{18.07, 34.0, 8.5\}$.

A step input is applied at $x = 0.0$ m and the closed-loop response $c(t)$ is analyzed for $x = 3.0$ m, without actuator saturation (Fig. 40). We verify that the system with a PID controller, tuned through the ZNOL heuristics, does not produce satisfactory results giving a significant overshoot ov and a large settling time t_s namely $\{t_s, t_p, t_r, ov(\%)\} \equiv \{44.8, 27.5, 12.0, 68.56\}$, where t_p represents the peak time and t_r the rise time. We analyze two indices that measure the response error, namely the integral square error (ISE) and the integral time square error (ITSE) criteria defined as:

$$\text{ISE}=\int_0^{\infty}\left[r(t)-c(t)\right]^2 dt \tag{32}$$

$$\text{ITSE}=\int_0^{\infty}t\left[r(t)-c(t)\right]^2 dt \tag{33}$$

We can use other performance criteria such as the integral absolute error (IAE) or the integral time absolute error (ITAE); however, in the present case the ISE and the ITSE criteria have produced the best results and are adopted in the study.

In this case, the PID reveals the following values for parameters (ISE, ITSE) = (27.53, 613.97).

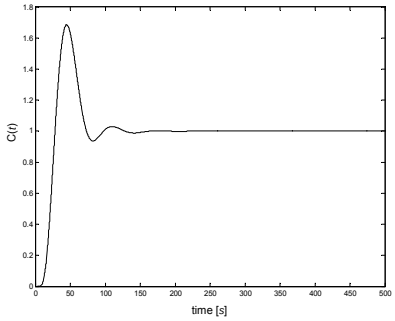

Figure 40 - step responses of the closed-loop system for the PID controller and $x = 3.0$ m.

ISBN: 978-972-99064-4-2

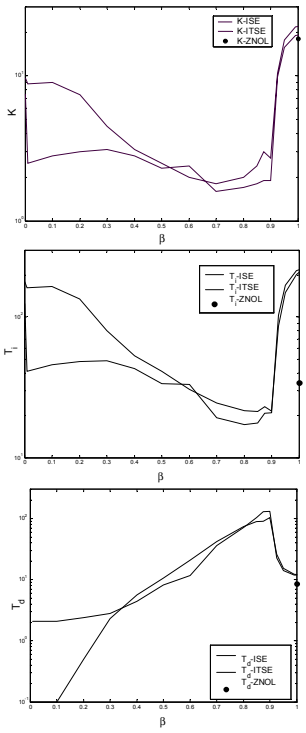

Figure 41 - the PID$^{\beta}$ parameters (K, T_i, T_d) versus β for the ISE and ITSE criteria. The dot represents the PID-ZNOL.

The poor results indicate again that the method of tuning may not be the most adequate for the control of the heat system.

In fact, the inherent fractional dynamics of the system lead us to consider other configurations. In this perspective, we propose the use of fractional controllers tuned by the minimization of the indices ISE and ITSE.

8.3 PID$^{\beta}$ tuning using optimization indices

In this sub-section we analyze the closed-loop system under the action of the PID$^{\beta}$ controller given by the transfer function (30) with $\alpha = 1$ and $0 \le \beta \le 1$. The fractional derivative term $T_d s^{\beta}$ in equation (30) is implemented through a 4th-order Padé discrete rational transfer function. It is used a sampling period of $T = 0.1$ s.

The PID$^{\beta}$ controller is tuned by the minimization of an integral performance index. For that purpose, we adopt the ISE and ITSE criteria.

A step reference input $R(s) = 1/s$ is applied at $x = 0.0$ m and the output $c(t)$ is analyzed for $x = 3.0$ m, without actuator saturation. The heat system is simulated for 3000 seconds. Figure 41 illustrates the variation of the fractional PID parameters (K, T_i, T_d) as function of the order's derivative β, for the ISE and the ITSE criteria. The dots represent the values corresponding to the classical PID addressed in the previous section.
The curves reveal that for $\beta < 0.4$ the parameters (K, T_i, T_d) are slightly different, for the two ISE and ITSE criteria, while for $\beta \ge 0.4$ they lead to almost similar values. This fact indicates a large influence of a weak order derivative on system's dynamics.

To further illustrate the performance of the fractional-order controllers a saturation nonlinearity is included in the closed-loop system of Fig. 39 and inserted in series with the output of the controller $G_c(s)$. The saturation element is defined as:

$$n(m) = \begin{cases} m, & |m| < \delta \\ \delta \operatorname{sign}(m), & |m| \ge \delta \end{cases} \qquad (34)$$

The controller performance is evaluated for $\delta = \{20, \ldots, 100\}$ and $\delta = \infty$ which corresponds to a system without saturation. We use the same fractional-PID parameters obtained without considering the saturation nonlinearity.

Figures 42 and 43 show the step responses of the closed-loop system and the corresponding controller output, for the PID$^{\beta}$ tuned in the ISE and ITSE perspectives for $\delta = 10$ and $\delta = \infty$, respectively. The controller parameters $\{K, T_i, T_d, \beta\}$ correspond to the minimization of those indices leading to the values ISE: $\{K, T_i, T_d, \beta\} \equiv \{3, 23, 90.6, 0.875\}$ and ITSE: $\{K, T_i, T_d, \beta\} \equiv \{1.8, 17.6, 103.6, 0.85\}$.

The step responses reveal a large diminishing of the overshoot and the rise time when compared with the integer PID, showing a good transient response and a zero steady-state error. The PID$^{\beta}$ leads to better results than the classical PID controller tuned through the ZNOL rule. These results demonstrate the effectiveness of the fractional algorithms when used for the control of fractional-order systems. The step response and the controller output are also improved when the saturation level δ is diminished.
Figure 44 depicts the ISE and ITSE indices for $0 \le \beta \le 1$, when $\delta = \{20, \ldots, 100\}$ and $\delta = \infty$. We verify the existence of a minimum for $\beta = 0.875$ and $\beta = 0.85$ for the ISE and ITSE cases, respectively. Furthermore, the higher the δ the lower the value of the index.

Figures 45 and 46 show the variation of the settling time t_s, the peak time t_p, the rise time t_r, and the percent overshoot ov(%), for the closed-loop response tuned through the minimization of the ISE and the ITSE indices, respectively.

In the ISE case t_s, t_p e t_r diminish rapidly for $0 \le \beta \le 0.875$, while for $\beta > 0.875$ the parameters increase smoothly. For the ITSE we verify the same behavior for $\beta = 0.85$. On the other hand, ov(%) increases smoothly for $0 \le \beta \le 0.7$, while for $\beta > 0.7$ it decreases very quickly, both for the ISE and the ITSE indices.

ISBN: 978-972-99064-4-2

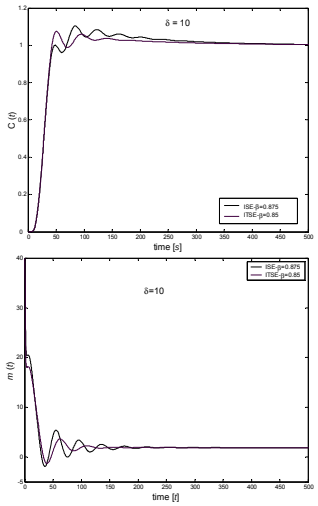

Figure 42 - step responses of the closed-loop system and the controller output for the ISE and the ITSE indices, with a PID$^{\beta}$ controller, $\delta = 10$ and $x = 3.0$ m.

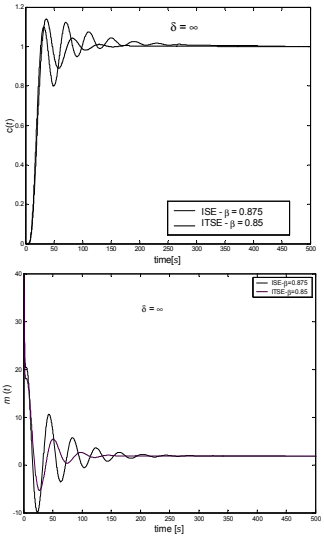

Figure 43 - step responses of the closed-loop system and the controller output for the ISE and the ITSE indices, with a PID$^{\beta}$ controller, $\delta = \infty$ and $x = 3.0$ m.

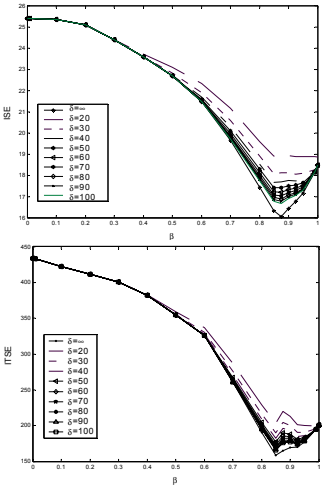

Figure 44 - ISE and ITSE versus $0 \le \beta \le 1$ for $\delta = \{20, ..., 100\}$ and $\delta = \infty$.

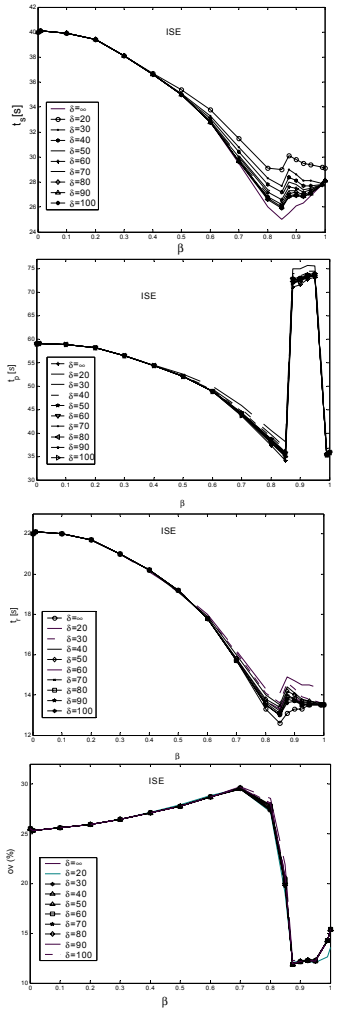

Figure 45 - parameters t_s, t_p, t_r, ov(%) for the step responses of the closed-loop system for the ISE indice, with a PID$^{\beta}$ controller, when $\delta = \{20, ..., 100\}$ and $\delta = \infty$, $x = 3.0$ m.

In conclusion, for $0.85 \le \beta \le 0.875$ we get the best controller tuning, superior to the performance revealed by the classical integer-order scheme.

9. Electrical impedance of fruits

In an electrical circuit the voltage $u(t)$ and the current $i(t)$ can be expressed as a function of time t:

$$u(t) = U_0 \cos(\omega t) \quad (35)$$

$$i(t) = I_0 \cos(\omega t + \phi) \quad (36)$$

where U_0 and I_0 are the amplitudes of the signals, ω is the frequency and ϕ is the current phase shift. The voltage and current can be expressed in complex form as:

$$u(t) = \mathrm{Re}\left\{U_0 e^{j(\omega t)}\right\} \quad (37)$$

$$i(t) = \mathrm{Re}\left\{I_0 e^{j(\omega t + \phi)}\right\} \quad (38)$$

ISBN: 978-972-99064-4-2

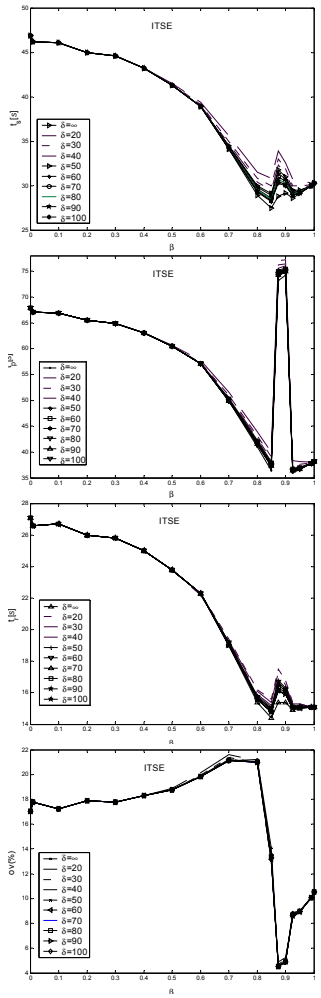

Figure 46 - parameters t_s, t_p, t_r, ov(%) for the step responses of the closed-loop system for the ITSE indice, with a PID$^{\beta}$ controller, when $\delta = \{20, ..., 100\}$ and $\delta = \infty$, $x = 3.0$ m.

Consequently, the electrical impedance $Z(j\omega)$ is:

$$Z(j\omega) = \frac{U(j\omega)}{I(j\omega)} = Z_0 e^{j\phi} \tag{39}$$

A brief reference about the constant phase elements (*CPE*) and Warburg impedance is presented here due to their application in the work. In fact, to model an electrochemical phenomenon it is often used a CPE because the surface is not homogeneous [46, 47]. So, with a *CPE*:

$$Z(j\omega) = \frac{1}{(j\omega)^{\alpha} C} \tag{40}$$

C is the capacitance, with units $[m^{-2/\alpha}\, kg^{-1/\alpha}\, s^{(\alpha+3)/\alpha}\, A^{2/\alpha}]$, and α is a parameter that can change between 0 and 1, being an ideal capacitor for $\alpha = 1$.

On the other hand, in electrochemical systems with diffusion, the impedance is modeled by the so-called Warburg element [47-49]. The Warburg element arises from one-dimensional diffusion of an ionic species to the electrode. If the impedance is under an infinite diffusion layer, the Warburg impedance is:

$$Z(j\omega) = \frac{R}{(j\omega)^{0.5} C} \tag{41}$$

where R is the diffusion resistance. If the diffusion process has finite length, the Warburg element becomes:

$$Z(j\omega) = R \frac{\tanh(j\omega\tau)^{0.5}}{(\tau)^{0.5}} \tag{42}$$

with $\tau = \delta^2 / D$, where R is the diffusion resistance, τ is the diffusion time constant, δ is the diffusion layer thickness and D is the diffusion coefficient.

9.1 Study of fractional order electrical impedances

The structure of fruits and vegetables has cells that are sensitive to heat, pressure and other stimuli. These systems constitute electrical circuits exhibiting a complex behavior. Bearing these facts in mind, in our work we study the electrical impedance for several botanical elements, under the point of view of fractional order systems.

We apply sinusoidal excitation signals $v(t)$, to the botanical system, for several distinct frequencies ω (Fig. 47) and the impedance $Z(j\omega)$ is measured based on the resulting voltage $u(t)$ and current $i(t)$. Moreover, we measure the environmental temperature, the weight, the length and width of all botanical elements. This criterion helps us to understand how these factors influence $Z(j\omega)$.

In this study we develop several different experiments for evaluating the variation of the impedance $Z(j\omega)$ with the amplitude of the input signal V_0, for different electrode lengths of penetration inside the element Δ, the environmental temperature T, the weights W and the dimension D.

The value of R is changed for each experiment, in order to adapt the values of the voltage and current to the scale of the measurement device.

We start by analyzing the impedance for an amplitude of input signal of $V_0 = 10$ volt, a constant adaptation resistance R_a = 15 kΩ, applied to one *Solanum Tuberosum* (potato), with an weight $W = 1.24\ 10^{-1}$ kg, environmental temperature $T = 26.5$ degree Celsius, dimension $D = 7.97\ 10^{-2} \times 5.99\ 10^{-2}$ m, and the electrode length penetration $\Delta = 2.1\ 10^{-2}$ m.

ISBN: 978-972-99064-4-2

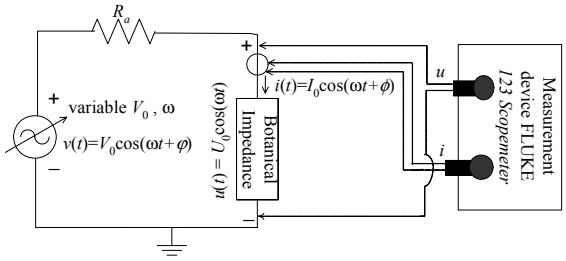

Figure 47 - electrical circuit for the measurement of the botanical impedance $Z(j\omega)$.

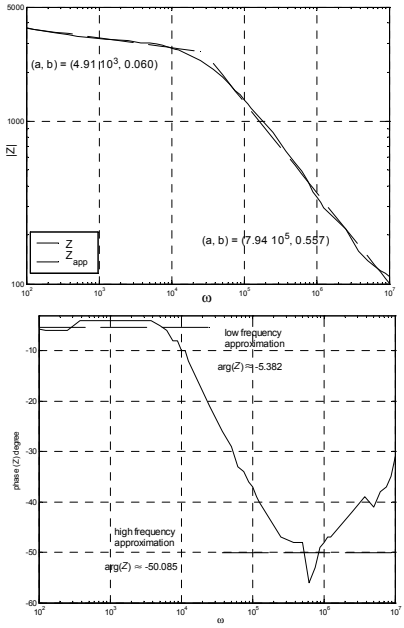

Figure 48 - Bode diagrams of the impedance $Z(j\omega)$ for the potato.

Figure 48 presents the Bode diagrams for $Z(j\omega)$. The results reveal that the system has fractional order impedance. In fact, approximating the experimental results in the amplitude Bode diagram through a power function namely by $|Z(j\omega)| = a\omega^{-b}$, we obtain $(a, b) = (4.91\ 10^3, 0.0598)$, at the low frequencies, and $(a, b) = (7.94\ 10^5, 0.5565)$, at the high frequencies.

It is interesting to compare the polar diagram and the admittance loci for *RLC*, series or parallel, circuits. We verify that our systems have similarities with the *RC* parallel circuit and, therefore, we conclude that this vegetable has proprieties similar to a kind of capacitor. In order to analyze the system linearity we evaluate $Z(j\omega)$ for different amplitudes of input systems, namely, $V_0 = \{5, 15, 20\}$ volt, maintaining constant the adaptation resistance $R_a = 15\ \text{k}\Omega$.

The impedance $Z(j\omega)$ has a fractional order and this characteristic does not change significantly with the variation of input signal amplitude (Table 9). Therefore, we can conclude that this system has a linear characteristic.

Table 9 - comparison of the values of $|Z(j\omega)| \approx a\omega^{-b}$ for different amplitudes of the input signal.

Amplitude (Volt)	*low* ω		*high* ω	
	a	*b*	*a*	*b*
5	$4.79\ 10^3$	0.062	$6.52\ 10^5$	0.542
10	$4.91\ 10^3$	0.060	$7.94\ 10^5$	0.557
15	$4.54\ 10^3$	0.054	$5.66\ 10^5$	0.530
20	$4.65\ 10^3$	0.055	$5.86\ 10^5$	0.530

In a second experiment, we vary the length Δ of the electrode penetration inside the potato, and we evaluate its influence upon the value of the impedance. Therefore, we adjust the electrode to $\Delta = 1.42\ 10^{-2}$ m, with $V_0 = 10$ volt and adaptation resistance $R_a = 5\ \text{k}\Omega$, leading to $|Z(j\omega)|$ approximations $(a, b) = (5.48\ 10^3, 0.0450)$, at the low frequencies, and $(a, b) = (1.00\ 10^6, 0.5651)$, at the high frequencies. With these results, we conclude that the length of wire inside the potato does not change significantly the values of the fractional orders. Also the linearity was again confirmed.

The last experiment with the potato is related with the variation of environmental temperature. In this case, we use the first potato and the same conditions of first experience, but with an temperature $T = 25.7$ degree Celsius. The amplitude impedance $|Z(j\omega)|$ has the values: $(a, b) = (8.91\ 10^3, 0.0555)$, at the low frequencies, and $(a, b) = (7.10\ 10^5, 0.5010)$, at the high frequencies. Once more we verify the small variation of the fractional order.

Another issue that may influence the results is the weight. Therefore, we apply an input signal with amplitude $V_0 = 10$ volt, adaptation resistance $R_a = 15\ \text{k}\Omega$, with environmental temperature $T = 26.5$ degree Celsius, and electrode penetration $\Delta = 2.1\ 10^{-2}$ m to another potato with dimension $D = 7.16\ 10^{-2} \times 3.99\ 10^{-2}$ m, weight $W = 5.89\ 10^{-2}$ kg. The asymptotic results for $|Z(j\omega)|$ are $(a, b) = (7.17\ 10^3, 0.0546)$, at the low frequencies and $(a, b) = (2.00\ 10^6, 0.5990)$, at the high frequencies. Again, this experience does not reveal significant variations in the fractional order while the linearity is also confirmed.

In conclusion, the impedance does not change significantly with the factors analyzed. In this line of thought, we organize similar experiments with other vegetables and fruits.

The results correspond to experiments adopting an amplitude of input signal $V_0 = 10$ volt and an electrode penetration $\Delta = 2.1\ 10^{-2}$ m. Similar experiments are developed for several fruits. Table 10 presents the characteristics of the vegetables and fruits respectively.

Figure 49 depicts Re $\{Z(j\omega)\}$ and Im $\{Z(j\omega)\}$ for some of the vegetables and fruits under study, and the corresponding approximation values. In these experiences, R_a is changed for each case.

ISBN: 978-972-99064-4-2

Table 10 - characteristics of the vegetables and fruits.

Vegetable or Fruit / Specie	*Weight* (kg)	*Length* (m)	*Width* (m)
Carrot / *Daucus Carota L.*	$8.85\ 10^{-2}$	$1.55\ 10^{-1}$	$3.39\ 10^{-2}$
Garlic / Allium sativum *L.*	$2.99\ 10^{-3}$	$1.38\ 10^{-2}$	$6.00\ 10^{-3}$
Onion / *Allium cepa L.*	$8.33\ 10^{-2}$	$5.86\ 10^{-2}$	$5.77\ 10^{-2}$
Potato / *Solanum tuberosum*	$1.24\ 10^{-1}$	$7.97\ 10^{-2}$	$5.99\ 10^{-2}$
Pimento / *Capsicum annuum*	$1.30\ 10^{-1}$	$1.23\ 10^{-1}$	$8.20\ 10^{-2}$
Tomato/*Lycopersicom esculentum*	$1.46\ 10^{-1}$	$5.57\ 10^{-2}$	$6.88\ 10^{-2}$
Turnip / *Brassica napobrassica*	$7.90\ 10^{-2}$	$7.26\ 10^{-2}$	$5.43\ 10^{-2}$
Apple / *Malus domestica*	$1.39\ 10^{-1}$	$6.36\ 10^{-2}$	$7.15\ 10^{-2}$
Banana / *Musa ingens*	$1.11\ 10^{-1}$	$1.49\ 10^{-1}$	$3.42\ 10^{-2}$
Kiwi / *Actinidia deliciosa*	$8.95\ 10^{-2}$	$6.52\ 10^{-2}$	$5.50\ 10^{-2}$
Lemon / *Citrus* × *limon*	$1.66\ 10^{-1}$	$9.19\ 10^{-2}$	$6.58\ 10^{-2}$
Orange / *Citrus sinensis*	$1.53\ 10^{-1}$	$6.69\ 10^{-2}$	$6.98\ 10^{-2}$
Pear / *Pyrus communis*	$9.72\ 10^{-2}$	$6.51\ 10^{-2}$	$5.63\ 10^{-2}$

The results reveal that $Z(j\omega)$ has distinct characteristics according with the frequency range. For low frequencies, the impedance is approximately constant, but for high frequencies, it is clearly of fractional order.

9.2 The impedance model

In the previous section we verified that it is difficult to find a model for $Z(j\omega)$ within the whole frequencies range. In this section, we apply the circuit of Fig. 50, often adopted in the area of electrochemistry, where R_0 and R_1 are resistances and *CPE* is given in equation (40).

The numerical values of R_0, R_1, C and α for the different impedances are shown in Table 11.

The results reveal a very good fit for several vegetables and fruits. Figure 51 presents the polar diagrams for the garlic, potato, tomato, kiwi and pear. It is clear that adopting circuits with more components, and other configuration, we can have better approximations. Therefore, in future development we will study new circuits for modeling the impedance of other materials.

Recent research focus on the implementation of fractional order capacitances, often called fractances. Patents and commercial products are presently available, opening promising areas of application in electronics and control [47].

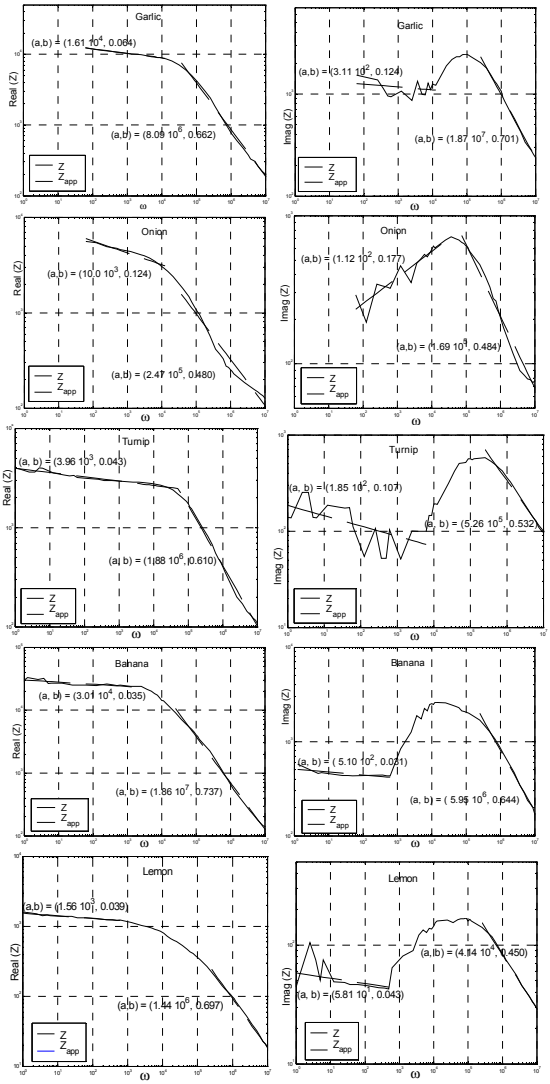

Figure 49 - diagrams of real Re $\{Z(j\omega)\}$ and imaginary Im $\{Z(j\omega)\}$ parts of the electrical impedance for several vegetables and fruits: garlic (with $R_a = 15.0\ \text{k}\Omega$), onion (with $R_a = 2.7\ \text{k}\Omega$), turnip (with $R_a = 2.2\ \text{k}\Omega$), banana (with $R_a = 5.5\ \text{k}\Omega$) and lemon (with $R_a = 750\ \Omega$).

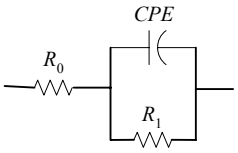

Figure 50 - the Randles circuit.

Table 11 - values of the elements of the Randles circuit for the garlic, potato, tomato, kiwi and pear.

Vegetable / fruits	$R_0\,[\Omega]$	$R_1\,[\Omega]$	C	α
Garlic	1	$9.7\ 10^{3}$	$1.81\ 10^{-7}$	0.609
Potato	57	$3.15\ 10^{3}$	$2.40\ 10^{-7}$	0.677
Tomato	35.04	240.30	$5.00\ 10^{-6}$	0.565
Kiwi	28.04	242.00	$7.67\ 10^{-6}$	0.531
Pear	44.04	409.00	$1.14\ 10^{-6}$	0.619

ISBN: 978-972-99064-4-2

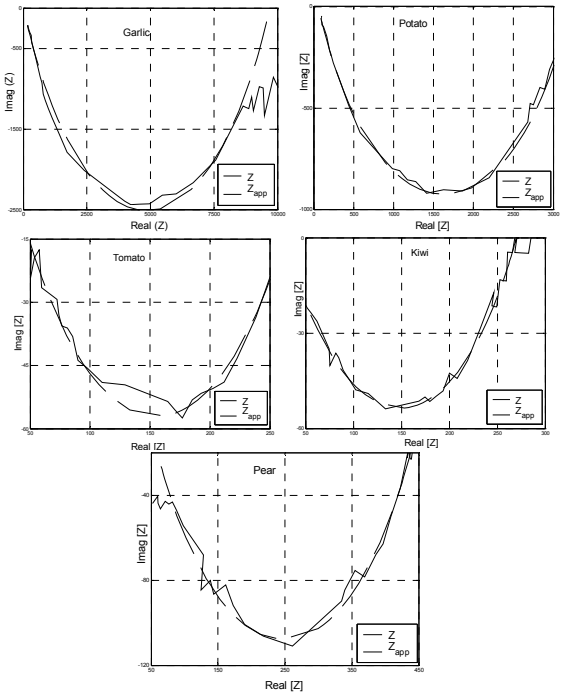

Figure 51 - polar diagrams of the impedance $Z(j\omega)$ for several vegetables and fruits: garlic, potato tomato, kiwi and pear.

This article follows an alternative strategy, studying natural living systems instead of technological artificial elements. Consequently, it points out interesting new directions towards the design of devices capable of measuring how mature is the fruit and vegetable, or to give an estimative of its life span for storage purposes.

10. Stock pricing dynamics

In this section are studied daily records of international stock prices [50, 51] using the Fourier transform and the Pseudo Phase Plane (*PPP*). It is analysed the unpredictability based on the power law of the decay of the Fourier transform. Several examples show the evidence that the S&P 500 Stock market is a persistent process, with long-run memory effects.

10.1 Spectral analysis of market indices

Several signals $x_i(t)$, $i \in \aleph$, ranging from 7910 trading-days in the same time period, were selected from the pool of the 500 biggest companies in US.

The Fourier transform is a mathematical tool [52] well adapted for analyzing the dynamics of the financial indices. The Fourier spectra $\mathrm{F}\{x_i(t)\}$ reveal a power decay that can be approximated by:

$$|\mathrm{F}\{x_i(t)\}| \approx c\ \omega^m,\ i \in \aleph,\ c,m \in \Re \qquad (43)$$

Figures 52 and 53 show the time series for three cases, and the corresponding Fourier transform with the approximation equation (43) that characterizes the decay slope, respectively. Table 12 depicts the ticker of the financial index and the corresponding spectral slopes m.

In Fig. 53 are also displayed the values of R^2, the square of the correlation factor between $ln(\omega)$ and $ln|\mathrm{F}\{x\}|$, that reflects the degree of statistical association of the pair of variables.

Figure 54 shows the relation between m and R^2, revealing that this association is almost functional.

10.2 Pseudo phase plane analysis

The *PPP* is a tool that makes easier the study of the time series dynamics by its representation in a 2D space [53, 54]. Once a delay d is selected the *PPP* is a plot of the points:

$$P_d = \left\{ \left(x_t, x_{t+d} \right) \in R^2 : t = 0,1,\cdots,N-d,\ 0 < d < N \right\} \qquad (44)$$

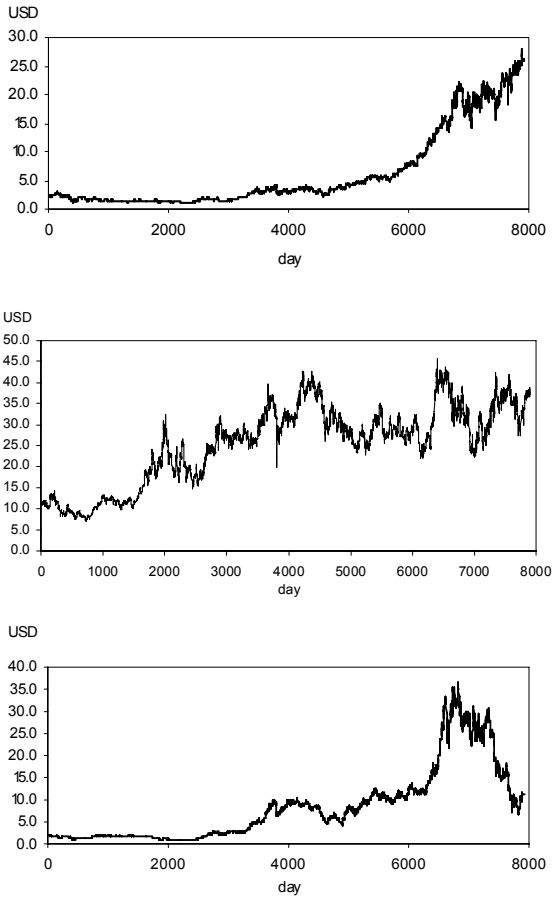

Figure 52 - plots of the time series of the financial indices ECL0, SUN0 and F0.

ISBN: 978-972-99064-4-2

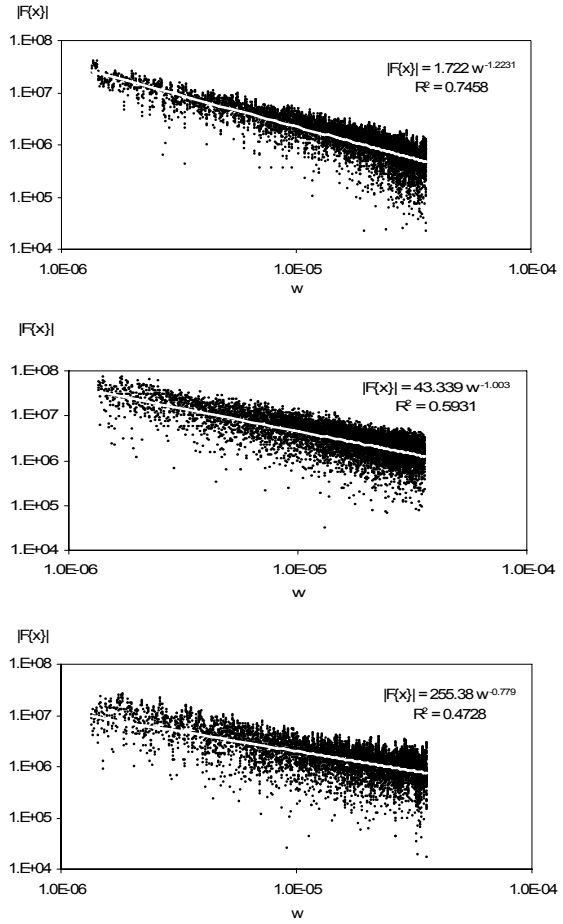

Figure 53 - plots of the Fourier transform of the financial indices ECL0, SUN0 and F0.

Table 12 - characteristics of five financial indices.

Ticker	*m*	dim_{PPP}	*d*
F0	–0.7790	1.463	1062
HPQ0	–0.8849	1.435	697
SUN0	–1.003	1.642	545
CTL0	–1.108	1.379	919
ECL0	–1.223	1.415	1043

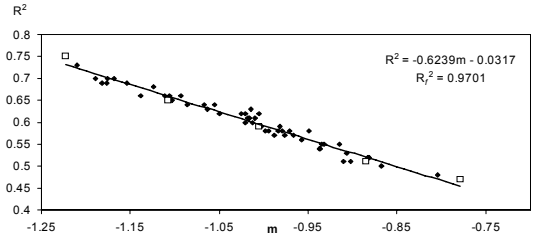

Figure 54 - plot of the decay slope *m versus* the correlation coefficient R^2 of the previous charts of the Fourier transform for several financial indices. The square marks represent the position of the five specific tickers under study.

A process, based on information theory, to determine the delay *d* that provides the best candidate for periodicity was proposed by [54, 55]. Several experiments revealed that an alternative, but simpler, way for selecting the delay is based in detecting the first contrasting minimum in the autocorrelation function (*ACF*) witch can be defined by the expression:

$$ACF(d) = \sum_{t=d}^{n} (x_t - \bar{x})(x_{t+d} - \bar{x}) \Big/ \sum_{t=d}^{n} (x_t - \bar{x})^2 \qquad (45)$$

As a drawback, this equivalent process must be done with the user supervision because, sometimes, due to the noise embedded in some financial signals the first minimum proposed by the computer program is not sufficient clear, and therefore must be seen as a false minimum.

In Fig. 55 are plotted the *ACF*s of three signals showing the first contrasting minima. The corresponding *PPP*s are represented in Fig. 56 and their fractal dimension dim_{PPP} is calculated.

The results reveal that the delay *d*, required for the *PPP* representation, and the fractal dimension dim_{PPP} [56] have a minimum and a maximum, respectively, when $m = -1$. A preliminary analysis indicates that this behavior is related with the unpredictable of the time series and to the nature of phenomena similar to biased random walks. A deeper understanding of the fractional or integer value of *m*, the fractal characteristics of the *PPP* and the signal predictability needs to be further explored.

Table 12 suggests a relationship between *m*, dim_{PPP} and *d*. These characteristics are clearly depicted in Fig. 57.

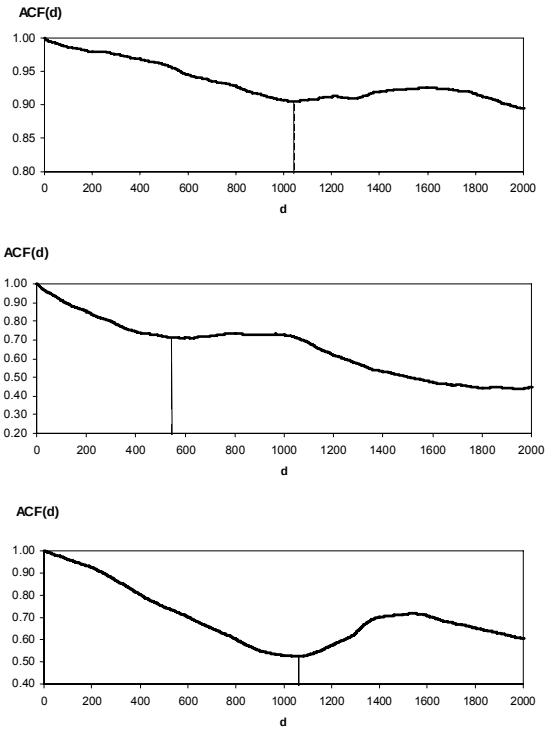

Figure 55 - plots of the *ACF* for the financial indices ECL0, SUN0 and F0.

ISBN: 978-972-99064-4-2

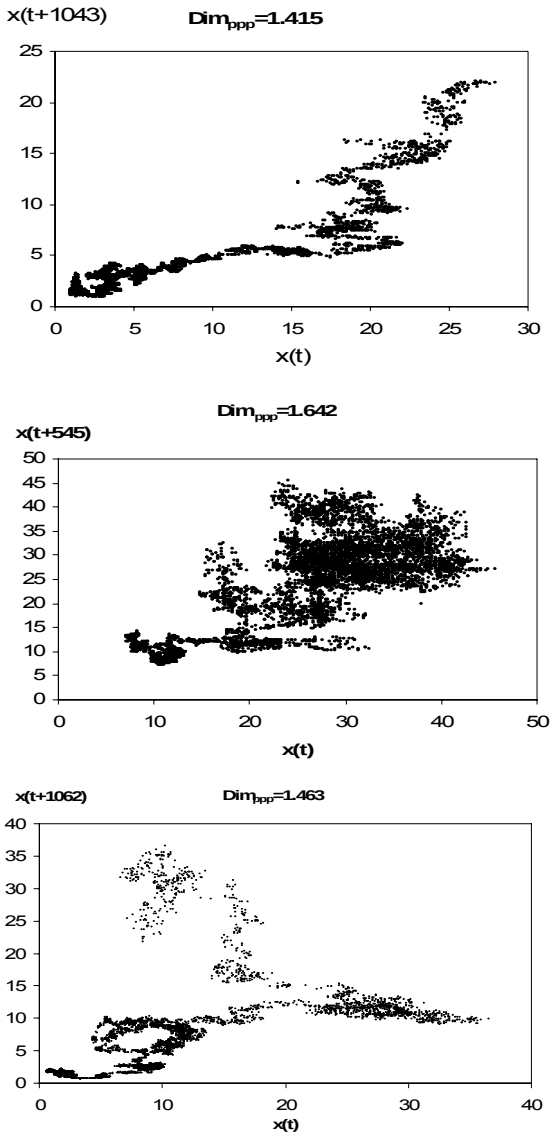

Figure 56 - plot of the *PPP* for the financial indices ECL0, SUN0 and F0.

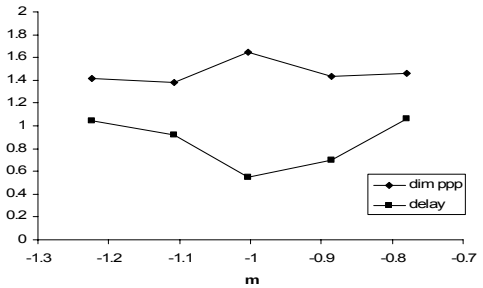

Figure 57 - plots of dim_{PPP} and *d versus m*.

11. Dynamics in a particle swarm optimization algorithm

This section studies the fractional dynamics during the evolution of a Particle Swarm Optimization (PSO) algorithm. Some swarm initial particles are randomly changed for stimulating the system response, and its effect is compared with a reference situation. The perturbation effect in the PSO evolution is observed in the perspective of the time behavior of the fitness of the best particle. The dynamics is investigated through the median of a sample of experiments, while adopting the Fourier analysis for describing the phenomena. The influence of the PSO parameters upon the global dynamics is also observed by performing several experiments for distinct values and parameters.

11.1 PSO algorithm

The particle swarm optimization algorithm was proposed originally by Kennedy and Eberhart [57]. This optimization technique is inspired in the way swarms (*e.g.*, flocks of birds, schools of fishes, herds) elements move in a synchronized way as a defensive tactic. An analogy is established between a particle and an element of swarm. The particle movement is characterized by two vectors representing its current position x and velocity v (Fig. 58).

11.2 The optimization system

This section presents the problem used in the study of the *optimization* PSO dynamic system. The objective function consists on minimizing the Easom function (46) [58]. This function has two parameter and the optimum has the value of $f(x_1,x_2)|_{opt}$=-1.0. The variables consist in x_1, $x_2 \in [-100,100]$ and the algorithm uses real code to represent the swarm.

$$f(x_1,x_2) = -\cos(x_1)\cos(x_2)\,\mathrm{e}^{-(x_1-\pi)^2-(x_2-\pi)^2} \quad (46)$$

A 50-population PSO is executed during 5000 generations under $\{\phi_1, \phi_2\} \sim U[0, 0.5]$.

The influence of several factors can be analyzed in order to study the dynamics of the PSO [60], particularly the inertia factor I or the ϕ_i maximum value, $i = \{1, 2\}$. This effect can vary according to the type of population size, fitness function, and generation number used in the PSO. In this work, it is changed randomly one particle of the initial population. The influence of the inertia parameter is studied by performing tests for the values $I = \{0.4, 0.5, \ldots, 0.9\}$. The fitness evolution of the best global particle is taken as the output signal.

```
Initialize Swarm
repeat
    forall particles do
     Calculate fitness f
     end
    forall particles do
    v_{t+1} = I v_t + φ1(b-x) + φ2(g-x)
    x_{t+1} = x_t + v_{t+1}
     end
until stopping criteria
```

Figure 58 - Particle Swarm Optimization.

ISBN: 978-972-99064-4-2

11.3 The PSO dynamics

The PSO system is stimulated by perturbing the initial population, namely by replacing one particle by a one new generated randomly. The corresponding swarm population fitness modification Δf is evaluated. The test condition remains unchanged during all the experiments. Therefore, the variation of the resulting PSO swarm fitness perturbation during the evolution can be viewed as the output signal that varies during the successive iterations. This analysis is evaluated using several experiments with different perturbation that replace the same particle in the population. All the other particles remain unchanged.

In this perspective, a perturbation input signal is created in the initial population when the replacement is performed. The output signal consists in the difference between the population fitness with and without the initial perturbation, that is $\Delta f(T) = f_{\text{pert}}(T) - \text{f}(T)$.

Once having de Fourier description of the output signals it is possible to calculate the corresponding normalized transfer function (47).

$$H(\text{j}w) = \frac{F\{\Delta f_i(T)\}(\text{j}w)}{F\{\Delta p_{m\ i}(T)\}(\text{j}w = 0)} \tag{47}$$

After repeating for all seeds a `representative' transfer function is obtained by using the median of the statistical sample [59] of n experiments for inertial term of I. In Fig. 59 are depicted the transfer functions for $I = 0.4$ up to $I = 0.9$.

After repeating for all seeds a `representative' transfer function is obtained by using the median of the statistical sample [59] of n experiments (see Fig. 59). The medians of the transfer functions calculated previously (*i.e.*, for each real and imaginary part and for each frequency) are taken as the final part of the numerical transfer function $H(\text{j}w)$.

Therefore, the median of the numerical system transfer functions, Fig. 59, is approximated by analytical expressions with gain $k = 1$, one pole $a \in \Re^+$ of fractional order $\alpha \in \Re^+$, and a time delay T, given by (48) (see Fig. 60).

$$G_l(\text{j}w) = \frac{k\,\text{e}^{-T}}{\left(\frac{\text{j}w}{a}+1\right)^{\alpha}} \tag{48}$$

For evaluating the influence of the inertia parameter I are performed several simulations ranging from $I = 0.4$ up to $I = 0.9$. The parameters of $\{a, \alpha, T\}$ are depicted in Fig. 61.

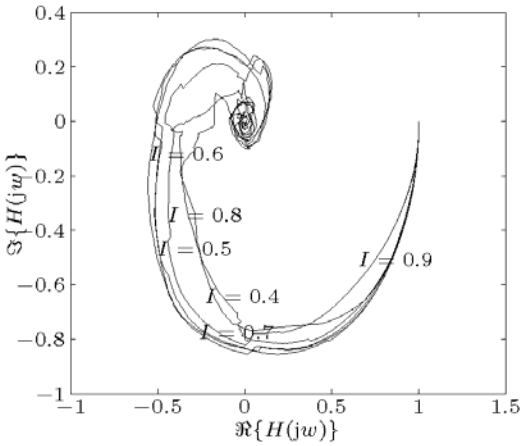

Figure 59 - median transfer function $H(\text{j}w)$ off the n experiments for $I = \{0.4,0.5,\ldots 0.9\}$.

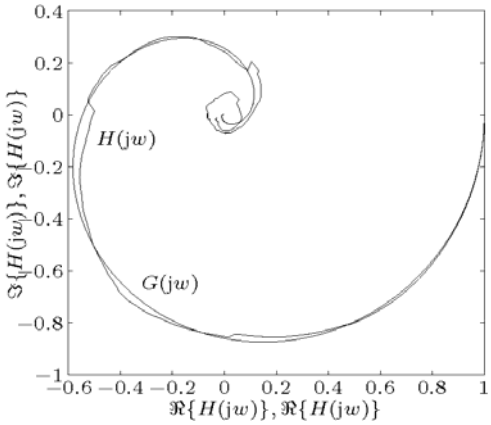

Figure 60 - polar diagram of $\{H(\text{j}w), G(\text{j}w)\}$ for $I = 0.6$.

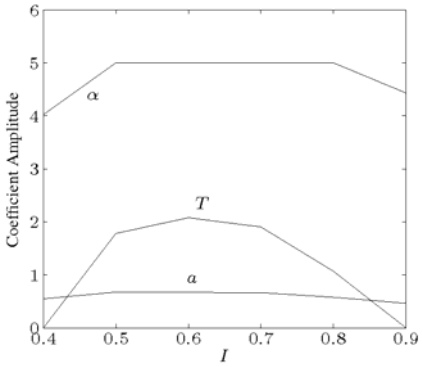

Figure 61 - parameters (a, α, T) of $G(\text{j}w)$.

The results reveal that the transfer function parameters $\{a, \alpha, T\}$ have some dependence with the inertia coefficient I. It can be observed that the parameters of transfer function have a maximum values at $I = 0.6$.

By enabling the zero/pole order to vary freely, we get non-integer values for α, while the adoption of an integer-order transfer function would lead to a larger number of zero/poles to get the same quality in the analytical fitting to the numerical values. The `requirement' of fractional-order models in

opposition with the classical case of integer models is a well-known discussion and even nowadays final conclusions are not clear since it is always possible to approximate a fractional frequency response through an integer one as long as we make use of a larger number of zeros and poles. Nevertheless, in the present experiments there is a complementary point of view towards FC.

This section analyzed the signal propagation and the dynamic phenomena involved in the time evolution of a swarm. The study was established on the basis of the Easom function optimization. While PSO schemes have been extensively studied, the influence of perturbation signals over the operating conditions is not well known.

Bearing these ideas in mind, the fractional calculus perspective calculus was introduced in order to develop simple, but comprehensive, approximating transfer functions of non-integer order.

12. Circuit synthesis using evolutionary algorithms

In recent decades evolutionary computation (EC) techniques have been applied to the design of electronic circuits and systems, leading to a novel area of research called Evolutionary Electronics (EE) or Evolvable Hardware (EH). EE considers the concept for automatic design of electronic systems. Instead of using human conceived models, abstractions and techniques, EE employs search algorithms to develop implementations not achievable with the traditional design schemes, such as the Karnaugh or the Quine-McCluskey Boolean methods.

Several papers proposed designing combinational logic circuits using evolutionary algorithms and, in particular, genetic algorithms (GAs) [61, 62] and hybrid schemes such as the memetic algorithms (MAs) [63].

Particle swarm optimization (PSO) constitutes an alternative evolutionary computation technique, and this paper studies its application to combinational logic circuit synthesis. Bearing these ideas in mind, the organization of this section is as follows. Sub-section 15.1 presents a brief overview of the PSO. Sub-section 15.2 describes the PSO based circuit design, while sub-section 15.3 exhibits the simulation results.

12.1 Particle swarm optimization

In the literature about PSO the term 'swarm intelligence' appears rather often and, therefore, we begin by explaining why this is so.

Non-computer scientists (ornithologists, biologists and psychologists) did early research, which led into the theory of particle swarms. In these areas, the term 'swarm intelligence' is well known and characterizes the case when a large number of individuals are able of accomplish complex tasks. Motivated by these facts, some basic simulations of swarms were abstracted into the mathematical field. The usage of swarms for solving simple tasks in nature became an intriguing idea in algorithmic and function optimization.

Eberhart and Kennedy were the first to introduce the PSO algorithm [64], which is an optimization method inspired in the collective intelligence of swarms of biological populations, and was discovered through simplified social model simulation of bird flocking, fishing schooling and swarm theory.

In the PSO, instead of using genetic operators, as in the case of GAs, each particle (individual) adjusts its flying according with its own and its companions experiences. Each particle is treated as a point in a D-dimensional space and is manipulated as described below in the original PSO algorithm:

$$v_{id} = v_{id} + c_1 rand()(p_{id} - x_{id}) + c_2 Rand()(p_{gd} - x_{id}) \quad (49a)$$

$$x_{id} = x_{id} + v_{id} \quad (49b)$$

where c_1 and c_2 are positive constants, *rand*() and *Rand*() are two random functions in the range [0,1], $X_i = (x_{i1}, x_{i2},\ldots, x_{iD})$ represents the ith particle, $P_i = (p_{i1}, p_{i2},\ldots, p_{iD})$ is the best previous position (the position giving the best fitness value) of the particle, the symbol g represents the index of the best particle among all particles in the population, and $V_i = (v_{i1}, v_{i2},\ldots, v_{iD})$ is the rate of the position change (velocity) for particle i.

Expression (49) represents the flying trajectory of a population of particles. Equation (49a) describes how the velocity is dynamically updated and equation (49b) the position update of the "flying" particles. Equation (49a) is divided in three parts, namely the momentum, the cognitive and the social parts. In the first part the velocity cannot be changed abruptly: it is adjusted based on the current velocity. The second part represents the learning from its own flying experience. The third part consists on the learning group flying experience [65].

The first new parameter added into the original PSO algorithm is the inertia weigh. The dynamic equation of PSO with inertia weigh is modified to be:

$$v_{id} = wv_{id} + c_1 rand()(p_{id} - x_{id}) + c_2 Rand()(p_{gd} - x_{id}) \quad (50a)$$

$$x_{id} = x_{id} + v_{id} \quad (50b)$$

ISBN: 978-972-99064-4-2

where w constitutes the inertia weigh that introduces a balance between the global and the local search abilities. A large inertia weigh facilitates a global search while a small inertia weigh facilitates a local search.

Another parameter, called constriction coefficient k, is introduced with the hope that it can insure a PSO to converge. A simplified method of incorporating it appears in equation (51), where k is function of c_1 and c_2 as it is presented in equation (52).

$$v_{id} = k\begin{bmatrix} v_{id} + c_1 rand(\ )(p_{id} - x_{id}) + \\ + c_2 Rand()(p_{gd} - x_{id}) \end{bmatrix} \quad (51a)$$

$$x_{id} = x_{id} + v_{id} \quad (51b)$$

$$k = 2\left(2 - \phi - \sqrt{\phi^2 - 4\phi}\right)^{-1} \quad (52)$$

where $\phi = c_1 + c_2$, $\phi > 4$.

There are two different PSO topologies, namely the global version and the local version. In the global version of PSO, each particle flies through the search space with a velocity that is dynamically adjusted according to the particle's personal best performance achieved so far and the best performance achieved so far by all particles. On the other hand, in the local version of PSO, each particle's velocity is adjusted according to its personal best and the best performance achieved so far within its neighborhood. The neighborhood of each particle is generally defined as topologically nearest particles to the particle at each side.

PSO is an evolutionary algorithm simple in concept, easy to implement and computationally efficient. Fig.s 62 – 64 present a generic EC algorithm, a hybrid algorithm, more precisely a MA and the original procedure for implementing the PSO algorithm, respectively.

The different versions of the PSO algorithms are: the real-value PSO, which is the original version of PSO and is well suited for solving real-value problems; the binary version of PSO, which is designed to solve binary problems; and the discrete version of PSO, which is good for solving the event-based problems. To extend the real-value version of PSO to binary/discrete space, the most critical part is to understand the meaning of concepts such as trajectory and velocity in the binary/discrete space.

Kennedy and Eberhart [64] use velocity as a probability to determine whether x_{id} (a bit) will be in one state or another (zero or one). The particle swarm formula of equation (49a) remains unchanged, except that now p_{id} and x_{id} are integers in [0.0,1.0] and a logistic transformation $S(v_{id})$ is used to accomplish this modification. The resulting change in position is defined by the following rule:

1. Initialize the population
2. Calculate the fitness of each individual in the population
3. Reproduce selected individuals to form a new population
4. Perform evolutionary operations such as crossover and mutation on the population
5. Loop to step 2 until some condition is met

Figure 62 - evolutionary computation algorithm.

1. Initialize the population
2. Calculate the fitness of each individual in the population
3. Reproduce selected individuals to form a new population
4. Perform evolutionary operations such as crossover and mutation on the population
5. Apply a local search algorithm
5. Loop to step 2 until some condition is met

Figure 63 - memetic algorithm.

1. Initialize population in hyperspace
2. Evaluate fitness of individual particles
3. Modify velocities based on previous best and global (or neighborhood) best
4. Terminate on some condition
5. Go to step 2

Figure 64 - particle swarm optimization process.

$$if\ [rand() < S(v_{id})] \quad then\ x_{id} = 1;\quad else\ x_{id} = 0 \quad (53)$$

where the function $S(v)$ is a sigmoid limiting transformation and $rand()$ is a random number selected from a uniform distribution in the range [0.0,1.0].

12.2 PSO based circuit design

We adopt a PSO algorithm to design combinational logic circuits. A truth table specifies the circuits and the goal is to implement a functional circuit with the least possible complexity. Four sets of logic gates have been defined, as shown in Table 13, being *Gset 2* the simplest one (*i.e.*, a RISC-like set) and *Gset 6* the most complex gate set (*i.e.*, a CISC-like set). Logic gate named WIRE means a logical no-operation.

In the PSO scheme the circuits are encoded as a rectangular matrix **A** ($row \times column = r \times c$) of logic cells as represented in Fig. 65.

Three genes represent each cell: <*input1*><*input2*><*gate type*>, where *input1* and *input2* are one of the circuit inputs, if they are in the first column, or one of the previous outputs, if they are in other columns. The gate type is one of the elements adopted in the gate set. The chromosome is formed with as many triplets as the matrix size demands (*e.g.*, triplets = $3 \times r \times c$). For example, the

ISBN: 978-972-99064-4-2

chromosome that represents a 3 × 3 matrix is depicted in Fig. 66.

The initial population of circuits (particles) has a random generation. The initial velocity of each particle is initialized with zero. The following velocities are calculated applying equation (50a) and the new positions result from using equation (50b). In this way, each potential solution, called particle, flies through the problem space. For each gene is calculated the corresponding velocity. Therefore, the new positions are as many as the number of genes in the chromosome. If the new values of the input genes result out of range, then a re-insertion function is used. If the calculated gate gene is not allowed a new valid one is generated at random. These particles then have memory and each one keeps information of its previous best position (*pbest*) and its corresponding fitness. The swarm has the *pbest* of all the particles and the particle with the greatest fitness is called the global best (*gbest*).

The basic concept of the PSO technique lies in accelerating each particle towards its *pbest* and *gbest* locations with a random weighted acceleration. However, in our case we also use a kind of mutation operator that introduces a new cell in 10% of the population. This mutation operator changes the characteristics of a given cell in the matrix. Therefore, the mutation modifies the gate type and the two inputs, meaning that a completely new cell can appear in the chromosome.

To run the PSO we have also to define the number P of individuals to create the initial population of particles. This population is always the same size across the generations, until reaching the solution.

The calculation of the fitness function F_s in equation (54) has two parts, f_1 and f_2, where f_1 measures the functionality and f_2 measures the simplicity. In a first phase, we compare the output Y produced by the PSO-generated circuit with the required values Y_R, according with the truth table, on a bit-per-bit basis. By other words, f_1 is incremented by one for each correct bit of the output until f_1 reaches the maximum value f_{10}, that occurs when we have a functional circuit. Once the circuit is functional, in a second phase, the algorithm tries to generate circuits with the least number of gates. This means that the resulting circuit must have as much genes <*gate type*> ≡ <*wire*> as possible. Therefore, the index f_2, that measures the simplicity (the number of null operations), is increased by *one* (*zero*) for each *wire* (*gate*) of the generated circuit, yielding:

$$f_{10} = 2^{ni} \times no \tag{54a}$$

$$f_1 = f_1 + 1 \text{ if } \{\text{bit } i \text{ of } \mathbf{Y}\} = \{\text{bit } i \text{ of } \mathbf{Y_R}\}, \quad i = 1, \ldots, f_{10} \tag{54b}$$

$$f_2 = f_2 + 1 \text{ if } \textit{gate type} = \textit{wire} \tag{54c}$$

$$F_s = \begin{cases} f_1, & F_s < f_{10} \\ f_1 + f_2, & F_s \geq f_{10} \end{cases} \tag{54d}$$

Table 13 - gate sets.

Gate Set	*Logic gates*
Gset 2	{AND,XOR,WIRE}
Gset 3	{AND,OR,XOR,WIRE}
Gset 4	{AND,OR,XOR,NOT,WIRE}
Gset 6	{AND,OR,XOR,NOT,NAND,NOR,WIRE}

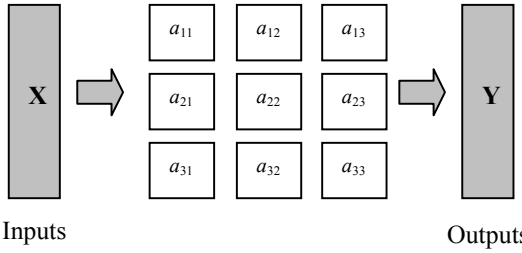

Figure 65 - a 3 × 3 matrix representing a circuit with input *X* and output *Y*.

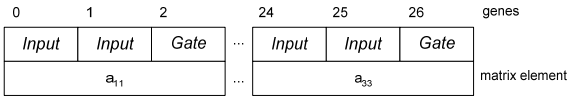

Figure 66 - chromosome for the 3 × 3 matrix of Fig. 65.

where *ni* and *no* represent the number of inputs and outputs of the circuit.

The concept of dynamic fitness function F_d results from an analogy between control systems and the GA case, where we master the population through the fitness function. The simplest control system is the proportional algorithm; nevertheless, there can be other control algorithms, such as, for example, the proportional and the differential scheme.

In this line of thought, expression (54) is a static fitness function F_s and corresponds to using a simple proportional algorithm. Therefore, to implement a proportional-derivative evolution the fitness function needs a scheme of the type [66]:

$$F_d = F_s + KD^{\mu}[F_s] \tag{55}$$

where $0 \leq \mu \leq 1$ is the differential fractional-order and $K \in \Re$ is the 'gain' of the dynamical term.

12.3 Experiments and results

A reliable execution and analysis of an EC algorithm usually requires a large number of simulations to provide a reasonable assurance that the stochastic effects are properly considered. Therefore, in this study are developed n = 20 simulations for each case under analysis.

The experiments consist on running the three algorithms {GA, MA, PSO} to generate a typical combinational logic circuit, namely a 2-to-1 multiplexer (*M2-1*), a 1-bit full adder (*FA1*), a 4-bit parity checker (*PC4*) and a 2-bit multiplier (*MUL2*), using the fitness scheme described in equations (54)

ISBN: 978-972-99064-4-2

and (55). The circuits are generated with the gate sets presented in Table 13 and $P = 3000$, $w = 0.5$, $c_1 = 1.5$ and $c_2 = 2$.

Figure 67 depicts the standard deviation of the number of generations to achieve the solution *S(N) versus* the average number of generations to achieve the solution *Av(N)* for the algorithms {GA, MA, PSO}, the circuits {*M2-1*, *FA1*, *PC4*, *MUL2*} and the gate sets {2, 3, 4, 6}. In this figure, we can see that the *MUL2* circuit is the most complex one, while the *PC4* and the *M2-1* are the simplest circuits. It is also possible to conclude that *Gset 6* is the less efficient gate set for all algorithms and circuits.

Figure 67 reveals that the plots follow a power law:

$$S(N) = a\left[Av(N)\right]^b \quad a,b \in \Re \qquad (56)$$

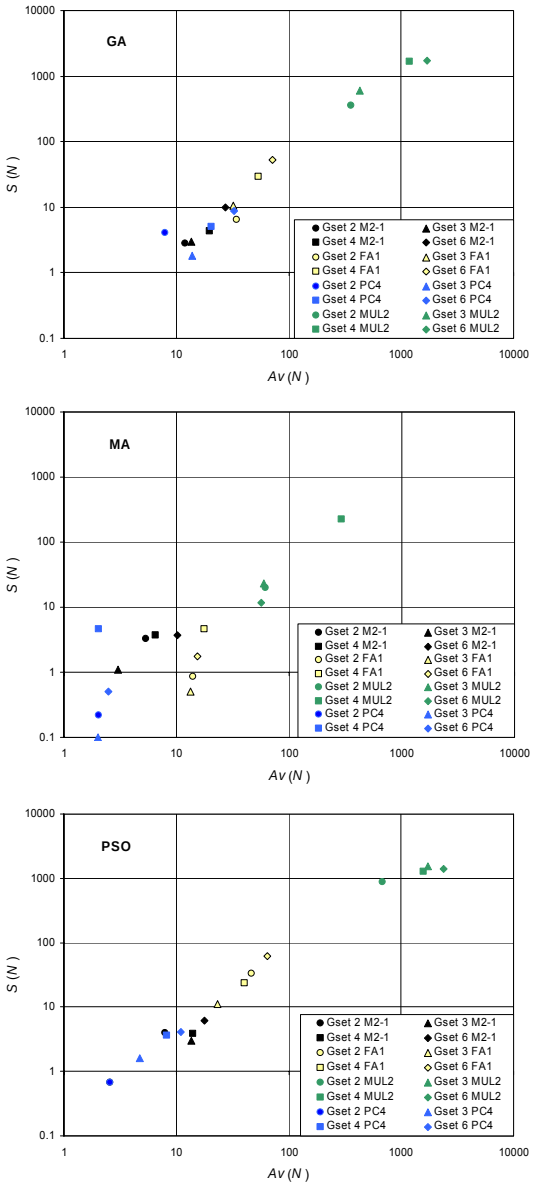

Figure 67 - *S*(*N*) *versus* *Av*(*N*) with $P = 3000$ and F_s for the GA, the MA and the PSO algorithms.

Table 14 - the Parameters (*a*, *b*) and (*c*, *d*).

Algorithm	*a*	*b*	*c*	*d*
GA	0.0365	1.602	0.1526	1.1734
MA	0.0728	1.2602	0.2089	1.3587
PSO	0.2677	1.1528	0.0141	1.1233

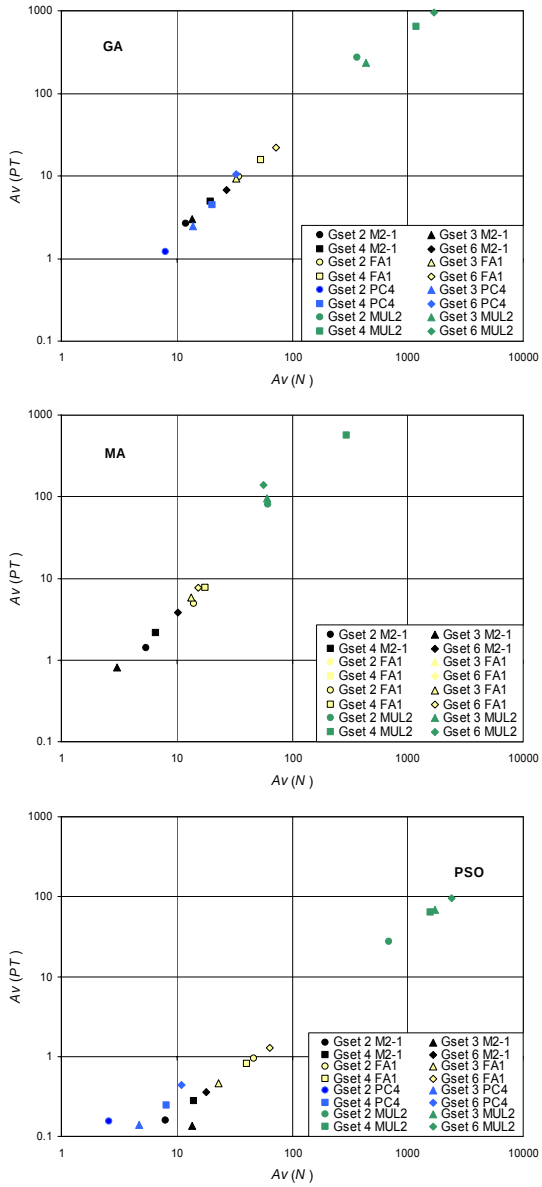

Figure 68 - *Av*(*PT*) *versus* *Av*(*N*) with $P = 3000$ and F_s for the GA, the MA and the PSO algorithms.

Table 14 presents the numerical values of the parameters (*a*, *b*) for the three algorithms.

In terms of *S*(*N*) *versus* *Av*(*N*), the MA algorithm presents the best results for all circuits and gate sets. In what concerns the other two algorithms, the PSO is superior (inferior) to the GA for complex (simple) circuits.

Figure 68 depicts the average processing time to obtain the solution *Av*(*PT*) *versus* the average number of generations to achieve the solution *Av*(*N*) for the algorithms {GA, MA, PSO}, the circuits

ISBN: 978-972-99064-4-2

{*M2-1, FA1, PC4, MUL2*} and the gate sets {2, 3, 4, 6}. When analysing these charts it is clear that the PSO algorithm demonstrates to be around ten times faster than the MA and the GA algorithms.

These plots follow also a power law:

$$Av(PT) = c\left[Av(N)\right]^d \quad c, d \in \Re \qquad (57)$$

Table 14 shows parameters (c, d) and we can see that the PSO algorithm has the best values.

Figures 69 and 70 depict the standard deviation of the number of generations to achieve the solution $S(N)$ and the average processing time to obtain the solution $Av(PT)$, respectively, *versus* the average number of generations to achieve the solution $Av(N)$ for the PSO algorithm using F_d, the circuits {*M2-1, FA1, PC4, MUL2*} and the gate sets {2, 3, 4, 6}. We conclude that F_d leads to better results in particular for the *MUL2* circuit and for the $Av(PT)$.

Figures 71 and 72 present a comparison between F_s and F_d.

In terms of $S(N)$ *versus* $Av(N)$ it is possible to say that the MA algorithm presents the best results. Nevertheless, when analysing Fig. 68, that shows $Av(PT)$ *versus* $Av(N)$ for reaching the solutions, we verify that the PSO algorithm is very efficient, in particular for the more complex circuits.

The PSO based algorithm for the design of combinational circuits follows the same profile as the other two evolutionary techniques presented in this paper.

Adopting the study of the *S(N) versus Av(N)* for the three evolutionary algorithms, the MA algorithm presents better results over the GA and the PSO algorithms. However, in what concerns the processing time to achieve the solutions the PSO outcomes clearly the GA and the MA algorithms. Moreover, applying the F_d the results obtained are improved further in all gate sets and in particular for the more complex circuits.

13. Conclusions

We have presented several applications of the FC concepts. It was demonstrated the advantages of using the FC theory in different areas of science and engineering. In fact, this paper studied a variety of different physical systems, namely:

- tuning of PID controllers using fractional calculus concepts;
- fractional PD$^{\alpha}$ control of a hexapod robot;
- fractional dynamics in the trajectory control of redundant manipulators;

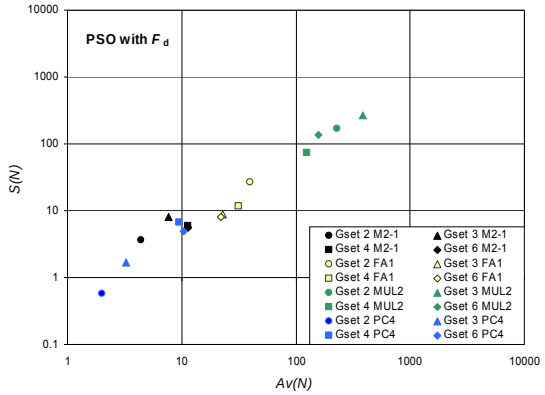

Figure 69 - $S(N)$ versus $Av(N)$ for the PSO algorithm, $P = 3000$ and F_d.

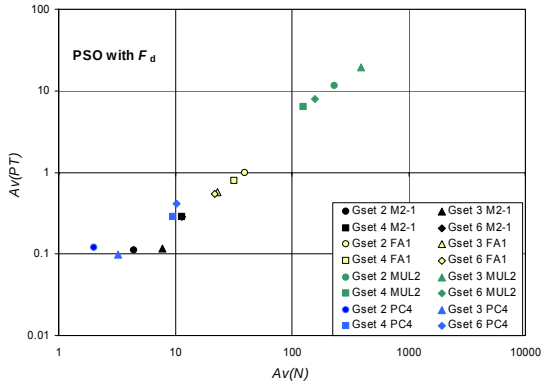

Figure 70 - $Av(PT)$ versus $Av(N)$ for the GA, $P = 3000$ and F_d.

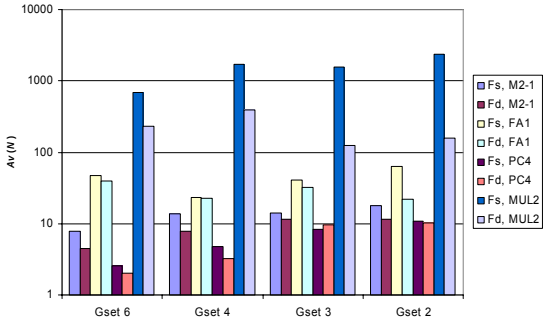

Figure 71 - $Av(N)$ for the PSO algorithm, $P = 3000$ using F_s and F_d.

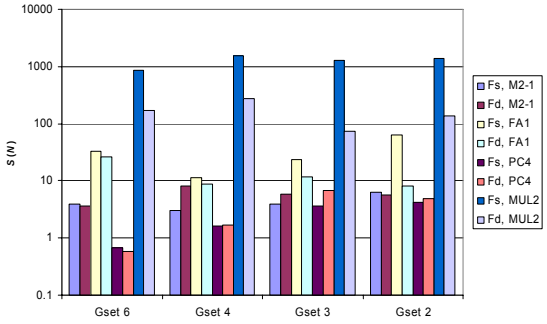

Figure 72 - $S(N)$ for the PSO algorithm, $P = 3000$ using F_s and F_d.

- fractional order Fourier spectra in robotic manipulators with vibrations;
- position/force control of a robotic manipulator;
- position/force control of two arms working in cooperation;
- heat diffusion;
- electrical impedance of fruits;
- stock pricing dynamics;
- dynamics in a particle swarm optimization algorithm;
- circuit synthesis using evolutionary algorithms.

The results demonstrate the importance of Fractional Calculus in the modeling and control of many systems and motivate for the development of new applications.

References

[1] K. B. Oldham, J. Spanier, *The Fractional Calculus*, Academic Press, New York, 1974.

[2] K. S. Miller, B. Ross, *An Introduction to the Fractional Calculus and Fractional Differential Equations*, Wiley & Sons, New York, 1993.

[3] I. Podlubny, *Fractional Differential Equations*, Academic Press, San Diego, 1999.

[4] R. Hilfer, *Applications of Fractional Calculus in Physics*, World Scientific, Singapore, 2000.

[5] A. Oustaloup, *La Commande CRONE: Commande Robuste d'Ordre Non Entier*, Editions Hermès, Paris, 1991.

[6] A. Oustaloup, *La Dérivation Non Entière: Théorie, Synthèse et Applications*, Editions Hermès, Paris, 1995.

[7] R. S. Barbosa, J. A. T. Machado, I. M. Ferreira, and J. K. Tar, "Dynamics of the Fractional – Order Van der Pol Oscillator," Proceedings of the ICCC 2004 – IEEE International Conference on Computational Cybernetics, Vienna, Austria, 2004.

[8] A. Charef, H. H. Sun, Y. Y. Tsao, and B. Onaral, "Fractal System Represented by Singularity Function," IEEE Transactions on automatic Control, Vol. 37, No. 9, pp. 1465-1470, 1992.

[9] M. F. Silva, J. A. T. Machado, and A. M. Lopes, "Comparison of Fractional and Integer Order Control of an Hexapod Robot", Proceedings of the VIB 2003 – ASME Int. 19th Biennial Conf. on Mechanical Vibration and Noise, USA, 2003.

[10] M. F. Silva, J. A. T. Machado, and R. S. Barbosa; "Complex-Order Dynamics in Hexapod Locomotion," Signal Processing – Special Section "Fractional Calculus Applications in Signals and Systems", Vol. 86, Issue 10, pp. 2785 – 2793, October 2006.

[11] M. F. Silva, J. A. T. Machado, and A. M. Lopes, "Modelling and Simulation of Artificial Locomotion Systems", ROBOTICA, Vol. 23, Issue 5, pp. 595 – 606, 2005.

[12] M. F. Silva, J. A. T. Machado, and A. M. Lopes, "Position / Force Control of a Walking Robot," MIROC – Machine Intelligence and Robot Control Vol. 5, pp. 33 – 44, 2003.

[13] M. F. Silva, J. A. T. Machado, "Fractional Order PD^{α} Joint Control of Legged Robots," Journal of Vibration and Control – Special Issue on "Modeling and Control of Artificial Locomotion Systems" Vol. 12; No. 12; pp. 1483 – 1501, 2006.

[14] E. Sahin Conkur, and Rob Buckingham, "Clarifying the Definition of Redundancy as Used in Robotics," Robotica, Vol. 15, pp. 583-586, 1997.

[15] S. Chiaverini, "Singularity-Robust Task-Priority Redundancy Resolution for Real Time Kinematic Control of Robot Manipulators," IEEE Trans. Robotics Automation Vol. 13, pp. 398-410, 1997.

[16] C.A Klein, C. C Huang, "Review of Pseudoinverse Control for Use With Kinematically Redundant Manipulators," IEEE Trans. Syst. Man, Cyber, Vol. 13, pp. 245-250, 1983.

[17] T. Yoshikawa, *Foundations of Robotics: Analysis and Control*, MIT Press, 1988.

[18] R Rodney Roberts, Anthony Maciejewski, "Singularities, Stable Surfaces and Repeatable Behavior of Kinematically Redundant manipulators," Int. Journal of Robotics Research Vol. 13, pp. 70-81, 1994.

[19] John Bay, "Geometry and Prediction of Drift-free trajectories for Redundant Machines Under Pseudoinverse Control," Int. Journal of Rob. Research Vol. 11, pp. 41-52, 1992.

[20] Y. Nakamura, *Advanced Robotics: Redundancy and Optimization*, Addinson-Wesley, 1991.

[21] Keith L. Doty, C. Melchiorri and C. Bonivento, "A Theory of Generalized Inverses Applied to Robotics," International Journal of Robotics Research Vol. 12, pp. 1-19, 1993.

[22] Bruno Siciliano, "Kinematic Control of Redundant Robot Manipulators: A Tutorial," Journal of Intelligent and Robotic Systems Vol. 3, pp. 201-212, 1990.

[23] W.J.Chung, Y. Youm, and W. K. Chung, "Inverse Kinematics of Planar Redundant Manipulators via Virtual Links with Configuration Index," J. of Robotic Systems Vol. 11, pp. 117-128, 1994.

[24] Sanjeev Seereeram, John T. Wen, "A Global Approach to Path Planning for Redundant Manipulators," IEEE Trans. Robotics Automation, Vol. 11, pp. 152-159, 1995.

[25] Fernando Duarte, J. A. Tenreiro Machado, "Chaotic Phenomena and Fractional-Order Dynamics in the Trajectory Control of Redundant Manipulators," Nonlinear Dynamics, Kluwer, Vol. 29, Nos. 1-4, pp. 315-342, 2002.

[26] J. Tenreiro Machado, "Analysis and design of fractional-order digital control systems," SAMS -Journal Systems Analysis-Modelling-Simulation Vol. 27, pp. 107-122, 1997.

[27] J. Tenreiro Machado, "Discrete-Time Fractional-Order Controllers," FCAA J. of Fractional Calculus & Applied Analysis, Vol. 4, pp. 47–66, 2001.

[28] Maria da Graça Marcos, Fernando B. M. Duarte, and J. A. Tenreiro Machado, "Complex Dynamics in the Trajectory Control of Redundant Manipulators," Nonlinear Science and Complexity, World Scientific, pp. 134-143, 2007.

[29] Miguel F. M. Lima, J.A. Tenreiro Machado, and Manuel Crisóstomo, "Experimental Set-Up for Vibration and Impact Analysis in Robotics," WSEAS Trans. on Systems, Issue 5, Vol. 4, pp. 569-576, May 2005.

[30] Miguel F. M. Lima, J.A. Tenreiro Machado, and Manuel Crisóstomo, "Fractional Order Fourier Spectra In Robotic Manipulators With Vibrations", Second IFAC Workshop on Fractional Differentiation and its Applications, Porto, Portugal, 2006.

[31] Oustaloup, Alain, Xavier Moreau, and Michel Nouillant, "From fractal robustness to non integer approach in vibration insulation: the CRONE suspension", Proc. of the 36th Conf. on Decision & Control, San Diego, CA, USA, December 1997.

[32] M. H. Raibert, J. J. Craig, "Hybrid Position/Force Control of Manipulators, " ASME Journal of Dynamic Systems, Measurement, and Control Vol. 102, No. 2, pp. 126-133, 1981.

[33] N. Hogan, "Impedance control: An Approach to Manipulation, Parts I-Theory, II-Implementation, III-Applications," ASME J. of Dynamic Systems, Measurement and Control Vol. 107, No. 1, pp. 1 –24, 1985.

[34] O. Khatib, "A Unified Approach for Motion and Force Control of Robot Manipulators: The Operational Space Formulation," IEEE J. of Rob. & Aut. Vol. 3, No. 1, pp. 43-53, 1987.

[35] B. Siciliano, L. Villani, "A Force/Position Regulator for Robot Manipulators without Velocity Measurements," IEEE Int. Conf. on Robotics and Automation, USA, 1996.

[36] N. M. Fonseca Ferreira, J. A. Tenreiro Machado, "Fractional-Order Hybrid Control of Robotic Manipulator", 11th IEEE Int. Conf. on Advanced Robotics, Coimbra, Portugal, 2003.

[37] Y. C. Tsai, A. H Soni, "Accessible Region and Synthesis of Robot Arms," ASME J. Mech. Design Vol. 103, pp. 803–811,1981.

[38] T. Yoshikawa, "Manipulability of Robotic Mechanisms," The Int. J. Robotics Research Vol. 4, pp. 3-9, 1985.

[39] H. Asada, "A Geometrical Representation of Manipulator Dynamics and its Application to Arm Design," ASME J. Dynamic Syst. Meas., Contr. Vol. 105, pp. 131–142, 1983.

[40] J. A. T. Machado, A. M. Galhano, "A Statistical and Harmonic Model for Robot Manipulators", Proc. of the IEEE Int. Conf. on Robotics and Automation, New Mexico, USA, 1997.

[41] Y. Nakamura, K. Nagai, and T. Yoshikawa, "Dynamics and Stability in Coordination of Multiple Robotic Mechanisms," Int. Journal of Robotics Research Vol. 8, pp. 44–61, 1989.

[42] N. M. Fonseca Ferreira, J. T. Machado, and J. Boaventura Cunha, "Fractional-Order Position/Force Robot Control", Proceedings of the 2nd IEEE Int. Conference on Computational Cybernetics, pp. 126-133, Vienna, Austria, 2004.

[43] R. Courant and D. Hilbert, *Methods of Mathematical Physics, Partial Differential Equations*, Wiley Interscience II, New York, 1962.

[44] J. T. Machado, Isabel Jesus, J. B. Cunha, and J. K. Tar, "Fractional Dynamics and Control of Distributed Parameter Systems," Intelligent Systems at the Service of Mankind Vol. 2, pp. 295-305, 2006.

[45] Isabel S. Jesus, Ramiro S. Barbosa, J. A. Tenreiro Machado, and J. Boaventura Cunha, "Strategies for the Control of Heat Diffusion Systems Based on Fractional Calculus", Proc. of the IEEE Int. Conf. on Comp. Cybernetics, Estonia, 2006.

[46] Evgenij Barsoukov, J. Ross Macdonald, *Impedance Spectroscopy, Theory, Experiment, and Applications*. John Wiley & Sons, Inc, 2005.

[47] I. S. Jesus, J. A. Tenreiro Machado, J. Boaventura Cunha, and Manuel F. Silva, "Fractional Order Electrical Impedance of Fruits and Vegetables", Proc. of the 25th IASTED Int. Conf. on Modelling, Identification and Control - MIC 2006,. Spain, February 2006.

[48] A. K. Jonscher, *Dielectric Relaxation in Solids*, Chelsea Dielectric Press, London, 1993.

[49] Samavati Hirad, Ali Hajimiri, Arvin R. Shahani, Gitty N. Nasserbakht, and Thomas H. Lee, "Fractal Capacitors,". IEEE Journal of Solid-State Circuits Vol. 33, No. 12, pp. 2035-2041, 1998.

[50] E.E. Peters, *Chaos and Order in Capital Market: A new view of cycles, prices and market volatility*, Wiley Finance Editions New York, 1996.

[51] J. A. Ramirez, M. Cisneros, C. Ibarra-Valdez, and A. Soriano, "Multifractal Hurst analysis of crude oil prices", Physica A Vol. 313, No. 3, ,pp. 651-670, October 2002.

[52] H. P Szu, *Applied Fourier Analysis*, University of Evansville, Harcourt Brace Jovanovitch, Publishers, New York, 1984.

[53] L. S. Liebovitch, *Fractals and Chaos Simplified for the Life Sciences*, Oxford University Press, inc, 1998.

[54] B.F. Feeny, "Fractional Derivatives Applied to Phase Space Reconstruction," J. of Nonlinear Dynamics Vol. 38, Nos. 1-2, December 2004.

[55] L. Trendafilova and H. van Brussel, "Nonlinear Dynamics tools for the motion Analysis and condition monitoring of Robot Joints," J. Mech. Systems and Signal Processing Vol. 15, No. 6, pp. 1141-1164, November 2001.

[56] K. Falconer, *Fractal Geometry Mathematical Foundation and Applications*, John Wiley & Sons, 2003.

[57] J. Kennedy, R. C. Eberhart, "Particle Swarm Optimization", Proceedings of the 1995 IEEE International Conference on Neural Networks, volume 4, pp. 1942-1948, Perth, Australia, IEEE Service Center, Piscataway, NJ, 1995.

[58] F. V. den Bergh, A. P. Engelbrecht, "A Study of Particle Swarm Optimization Particle Trajectories," Inf. Sci. Vol. 176, No. 8, pp. 937-971, 2006.

[59] J. A. Tenreiro Machado, A. M. S. F. Galhano, "A Statistical Perspective to the Fourier Analysis of Mechanical Manipulators," Journal Systems Analysis-Modelling-Simulation Vol. 33, pp. 373-384, 1998.

[60] E. J. Solteiro Pires, J. A. Tenreiro Machado, and P. B. de Moura Oliveira, "Dynamical Modelling of a Genetic Algorithm," Signal Processing Vol. 86, No. 10, pp. 2760-2770, 2006.

[61] S. J. Louis, Rawlins, and G. J. Designer, "Genetic Algorithms: Genetic Algorithms in Structure Design", Proc. of the Fourth Int. Conference on Genetic Algorithms, 1991.

[62] D. E. Goldberg, *Genetic Algorithms in Search Optimization and Machine Learning*, Addison-Wesley, 1989.

[63] Cecília Reis, J. A. Tenreiro Machado, and J. Boaventura Cunha, "An Evolutionary Hybrid Approach in the Design of Combinational Digital Circuits," WSEAS Transactions on Systems Vol. 4, Issue 12, pp. 2338-2345, December 2005.

[64] J. Kennedy, R. C. Eberhart, "Particle Swarm Optimization", Proceedings of the IEEE International Conference Neural Networks, pp. 1942-1948, November 1995.

[65] Y. Shi, R. C. Eberhart, "A Modified Particle Swarm Optimizer," Proceedings of the 1998 International Conf. on Evolutionary Computation, pp. 69-73, May 1998.

[66] C. Reis, J. Machado, and J. Cunha, "Evolutionary Design of Combinational Circuits Using Fractional-Order Fitness", Proceedings of the Fith EUROMECH Nonlinear Dynamics Conference, pp. 1312–1321, 2005.

Author(s) address

Department of Electrical Engineering,
Instituto Superior de Engenharia do Porto,
Rua Dr. António Bernardino de Almeida, 431
4200-072 Porto, Portugal